REPORT DOCUMENTATION PAGE

AFRL-SR-BL-TR-01-

0372

Public reporting burden for this collection of information is estimated to average 1 hour per response, including the time for reviewin ... ing the
data needed, and completing and reviewing this collection of information. Send comments regarding this burden estimate or any ot ... educing
this burden to Department of Defense, Washington Headquarters Services, Directorate for Information Operations and Reports (070 ... 202-
4302. Respondents should be aware that notwithstanding any other provision of law, no person shall be subject to any penalty for f ... urrently
valid OMB control number. **PLEASE DO NOT RETURN YOUR FORM TO THE ABOVE ADDRESS.**

1. REPORT DATE *(DD-MM-YYYY)*
05/24/01

2. REPORT TYPE
Contractor Report

3. DATES COVERED *(From - To)*
11/16/99 – 11/15/00

4. TITLE AND SUBTITLE
Effects of Shocks on the Unsteady Heat Transfer in a Film-Cooled Transonic Turbine Cascade

5a. CONTRACT NUMBER
AFOSR F49620-00-1-0024

5b. GRANT NUMBER
N/A

5c. PROGRAM ELEMENT NUMBER
N/A

6. AUTHOR(S)
Tom Diller, Wing Ng, Andrew Nix

5d. PROJECT NUMBER
N/A

5e. TASK NUMBER
N/A

5f. WORK UNIT NUMBER
N/A

7. PERFORMING ORGANIZATION NAME(S) AND ADDRESS(ES)

Mechanical Engineering Department
Virginia Tech, MC 0238
Blacksburg, VA 24061

8. PERFORMING ORGANIZATION REPORT NUMBER

9. SPONSORING / MONITORING AGENCY NAME(S) AND ADDRESS(ES)
Dr. Tom Beutner
AFOSR/NA
801 N. Randolph St., Rm 732
Arlington, VA 22203-1977

10. SPONSOR/MONITOR'S ACRONYM(S)

11. SPONSOR/MONITOR'S REPORT NUMBER(S)

12. DISTRIBUTION / AVAILABILITY STATEMENT

unlimited

20010625 172

13. SUPPLEMENTARY NOTES
None

14. ABSTRACT

An experimental program was performed to study the effects of high strength shocks on the film cooling heat transfer in a transonic turbine blade. Shocks stronger than seen in actual engines were generated by a shock tube and directed to pass into the cascade upstream of a linear set of blades. The results indicate that the increased strength of the shocks do not disrupt the boundary layer on the blade. Therefore, the heat transfer is still predictable by the methods determined for lower strength shocks, as reported in the attached two papers (presented in Munich during this research program). As a transition to work on high free-stream turbulence effects, initial results for a blown grid were obtained in low speed flow. The corresponding report is attached, but has not yet been published.

15. SUBJECT TERMS
gas turbine, heat transfer

16. SECURITY CLASSIFICATION OF: none			**17. LIMITATION OF ABSTRACT**	**18. NUMBER OF PAGES**	**19a. NAME OF RESPONSIBLE PERSON** Tom Diller
a. REPORT	**b. ABSTRACT**	**c. THIS PAGE**	none	36	**19b. TELEPHONE NUMBER** *(include area code)* 540-231-7198

Standard Form 298 (Rev. 8-98)
Prescribed by ANSI Std. Z39.18

Contract Report on

Effects of Shocks on the Unsteady Heat Transfer in a Film-Cooled Transonic Turbine Cascade

AFOSR F49620-00-1-0024

for the period
November 16, 1999 to November 15, 2000

submitted to

Program Manager
Dr. Tom Beutner
AFOSR/NA
801 N Randolph St., Rm 732
Arlington, VA 22203-1977

submitted by

Tom Diller, Wing Ng, Andrew Nix
Mechanical Engineering Department
Virginia Tech, MC 0238
Blacksburg, VA 24061

May 2001

TESTING OF AN ACTIVELY BLOWN GRID FOR GENERATION OF HIGH FREESTREAM TURBULENCE

Andrew C. Nix
anix@vt.edu
Graduate Research Assistant

Dr. T.E. Diller and Dr. W.F. Ng

Department of Mechanical Engineering
Virginia Tech, Blacksburg, VA

Abstract

This report presents the results of initial testing of an actively blown grid for producing high-intensity, large length-scale freestream turbulence for use in a linear, transonic turbine cascade. The design was achieved using data presented in the work of several other researchers.[1,2,3,4,5] The desired turbulence intensity (Tu%) and integral length scale (Λ_x) to match gas turbine engine conditions with similarity are Tu ≈ 15-20% and $\Lambda_x \approx 4$ cm. The testing stage of this work was performed in a low speed test section of similar flow area as the turbine cascade. Data are presented for the grid both with and without active blowing. The grid data without blowing was compared to correlations of turbulence and length scale decay presented by Roach[6] and Baines and Peterson[7] with good agreement for turbulence intensity decay and fair for length scale dispersion. Initial tests achieved a turbulence intensity of approximately 17% and a length scale of approximately 3.5 cm at a distance of 18 bar widths downstream of the blown grid.

Introduction

Using design ideas from published literature[1,2,3,4,5], an actively blown turbulence generating grid was developed incorporating both upstream and downstream blowing to generate large length-scale, high intensity freestream turbulence for use in a 6" span transonic turbine cascade. The generator (shown in Figure 1) has been designed to produce freestream turbulence with a turbulence intensity (Tu%) of approximately 15-20% with an integral length scale of 4 cm. This turbulence level (intensity and scale) was determined through research done at NASA Glenn by Dr. Jim Van Fossen, et al[8]. Van Fossen used a 60° section of a GE 90 combustor in a wind tunnel to model the exit flow of a combustor, including inlet swirl vanes, film cooling holes and dilution holes. All three of these combustor components contribute strongly to the combustor exit turbulence conditions. Hot wire surveys were performed downstream of the combustor to characterize the turbulence conditions at the exit. Combustion was not included, but previous research by Moss and Oldfield[9] showed that turbulence intensity and length scale were not significantly affected by the presence of combustion. Using Van Fossen's results, the desired length scale was increased to match the chord length of the blades

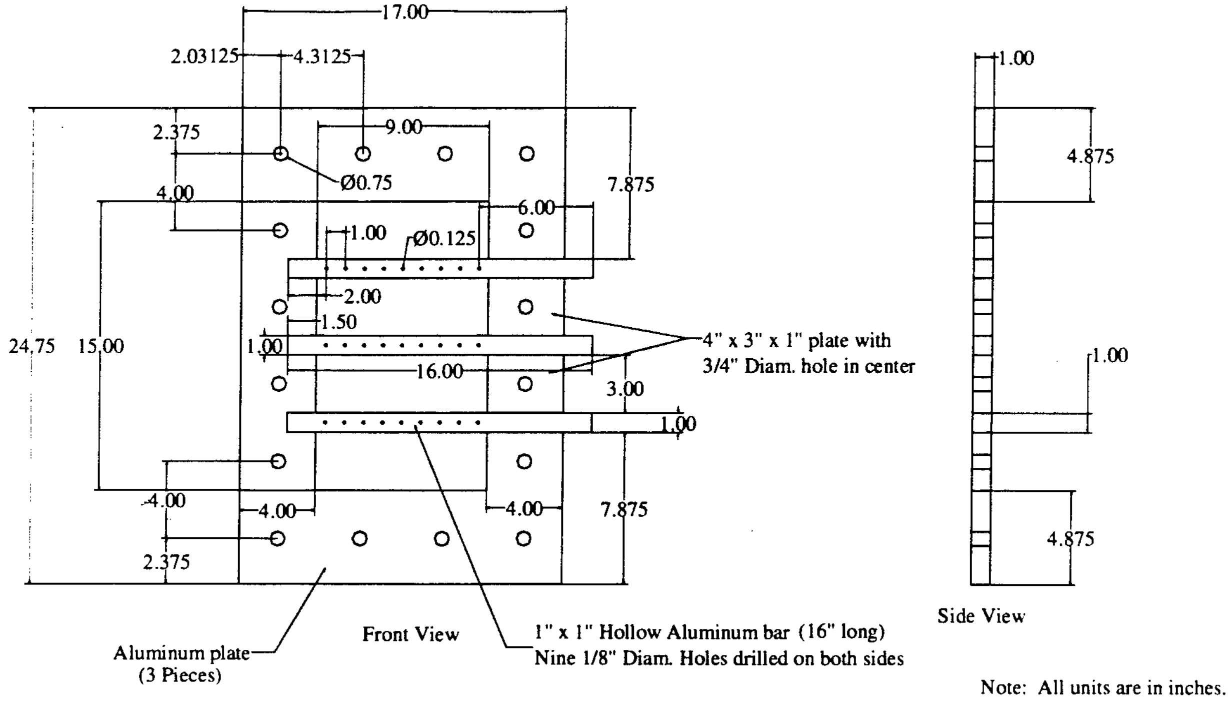
17.00
2.03125
4.3125
2.375
9.00
Ø0.75
7.875
4.00
6.00
1.00
Ø0.125
2.00
1.50
24.75
15.00
1.00
16.00
4" x 3" x 1" plate with
3/4" Diam. hole in center
3.00
1.00
4.00
4.00
4.00
7.875
2.375
Aluminum plate
(3 Pieces)
Front View
1" x 1" Hollow Aluminum bar (16" long)
Nine 1/8" Diam. Holes drilled on both sides
1.00
4.875
1.00
4.875
Side View
Note: All units are in inches.

Figure 1: Schematic of Actively-Blown Turbulence Generating Grid

used in the Virginia Tech transonic turbine cascade facility with similarity to the blades of a GE 90 engine. Van Fossen reported length-scales between 1 and 1.5 cm from his combustor simulation, where the chord length of a first stage GE 90 turbine blade is estimated as approximately 2 in (5.08 cm). Our turbine blade has a chord length of 5.4 in (13.72 cm), so the turbulent length scale desired was determined to be approximately 4 cm. Testing of the grid was performed in a low speed environment to characterize the turbulence from the grid. The mass flow ejected from the grid holes was adjusted in an attempt to reach the turbulence intensity and length scale desired. The momentum flux ratios (blowing vs. freestream) can then be matched in the transonic facility to hopefully achieve the same results in both environments (low-speed versus transonic).

The test setup for the low-speed tests is shown in Figure 2. The setup includes a 5 HP blower attached to several transition pieces, followed by a test section. The blower created mainstream flow velocities of approximately 20 m/s, whereas the inlet velocity of the transonic wind tunnel is approximately 100 m/s. The first transition piece changes the cross section of the flow path from circular to rectangular, the second transition piece changes the area to accommodate the turbulence generating grid and the third transition changes the flow area from the cross section of the grid to the cross section of the transonic wind tunnel test section, which is 12 inches high by 6 inches wide. All transition pieces were designed to avoid flow separation. A Plexiglas test section, which has this same cross-sectional geometry and is 20 inches in length, was fabricated to take data downstream of the turbulence grid in the low-speed environment. Initial testing of the blower through downstream hotwire velocity traverses indicated that the background freestream turbulence levels from the blower were very high (approximately 12%). To lower the background level of turbulence entering the test section, a flow straightener section was installed which consists of a section of honey comb, followed by a fine mesh

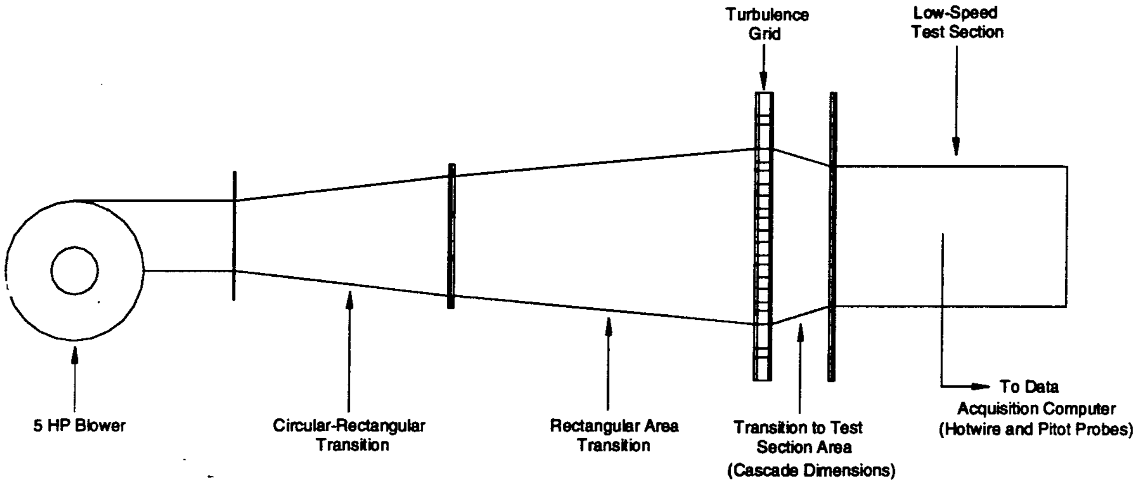
Turbulence Grid
Low-Speed Test Section
To Data Acquisition Computer (Hotwire and Pitot Probes)
5 HP Blower
Circular-Rectangular Transition
Rectangular Area Transition
Transition to Test Section Area (Cascade Dimensions)

Figure 2: Test Setup for Low Speed Testing of Turbulence Grid

screen, then a straight section 12 inches in length followed by another section of honeycomb. This flow straightener was installed just upstream of the rectangular transition piece in Figure 2. Background turbulence levels were decreased to slightly less than 2%.

Blowing air for the turbulence generating grid is supplied through high-pressure lines to a plenum tank. The plenum then supplies air to each of the three blowing bars (each square bar is 1" on a side) of the grid. A diagram of the blowing supply setup is shown in Figure 3. The grid has 1/8 in diameter holes drilled on both the upstream and downstream sides, spaced 1 inch apart. The bar spacing was set to 3 inches based on a combination of results from other researchers mentioned earlier.

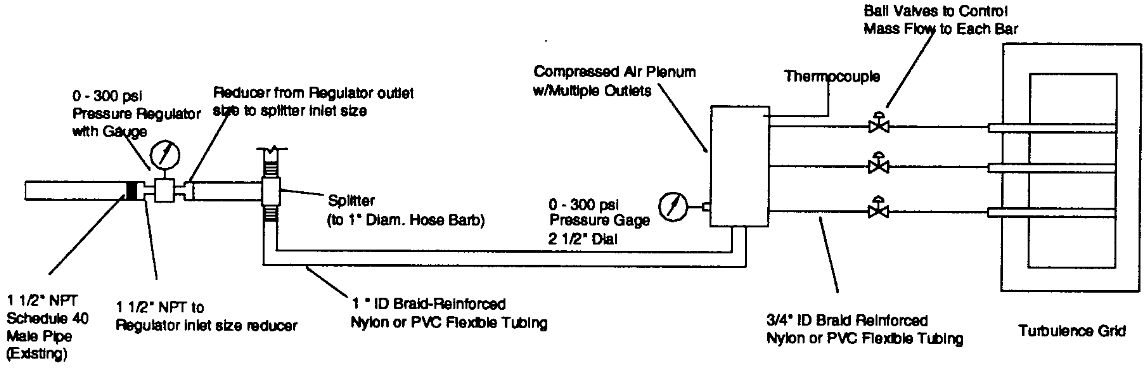
Ball Valves to Control Mass Flow to Each Bar
0 - 300 psi Pressure Regulator with Gauge
Reducer from Regulator outlet size to splitter inlet size
Compressed Air Plenum w/Multiple Outlets
Thermocouple
Splitter (to 1" Diam. Hose Barb)
0 - 300 psi Pressure Gage 2 1/2" Dial
1 1/2" NPT Schedule 40 Male Pipe (Existing)
1 1/2" NPT to Regulator inlet size reducer
1 " ID Braid-Reinforced Nylon or PVC Flexible Tubing
3/4" ID Braid Reinforced Nylon or PVC Flexible Tubing
Turbulence Grid

Figure 3: Diagram of Blowing Air Supply System

Velocity measurements (including fluctuating component) were taken at various locations throughout the test section using a hot wire anemometer probe. The probe was manually traversed vertically at one downstream location to demonstrate flow uniformity (checking if wakes are present from bars on grid) in the test section. This traverse was performed at 13 bar widths downstream of the grid. Four locations in the streamwise direction downstream of the grid were chosen to take data in the center of the passage in the absence of an adequate traversing system (to be added soon). Statistical and spectral analysis of the velocity data at these four locations was used to calculate the turbulence intensity and length-scale and the decay/dispersion of these quantities as the flow progresses through the test section. The data were sampled at 20 kHz, filtered at 10 kHz and AC coupled with a 5V offset to increase dynamic resolution. All data points were sampled for 6 s and 4 samples were taken at each point for averaging purposes.

From pressure and temperature measurements at the plenum and grid blowing hole exit, which have not yet been performed, the momentum flux ratio (blowing/freestream) can be determined for the low speed tests. The momentum flux ratio will be useful for matching turbulence characteristics when the turbulence grid is placed in the flow field of the transonic tunnel for use in turbine blade heat transfer testing.

Results

Characterization of Turbulence : Statistical and Spectral Analysis of Velocity Data

In order to characterize the turbulence from the developed actively blown grid, statistical and spectral analyses were performed on all data, both with and without blowing activated. Velocity data at each sampled point in the flowfield was actually averaged over 6 data samples to give better statistics and spectra. Statistical and spectral analyses included calculation of the mean velocity (U), fluctuating component of velocity (u), root mean square (RMS) of the fluctuating component of velocity (u'), autocorrelation (R_v), probability density functions (PDF), and power spectral density (PSD) calculations.

The streamwise instantaneous velocity signal can be decomposed into a mean and fluctuating component as follows:

$$\tilde{u} = U + u$$

where U is the mean velocity and u is the fluctuating component of velocity. The mean, fluctuating component and RMS of the discretized velocity data were calculated as follows:

$$U = \frac{1}{T}\int_{t=0}^{T} \tilde{u}\,dt = \frac{1}{N}\sum_{i=1}^{N} \tilde{u}_i$$

$$u = \tilde{u} - \frac{1}{N}\sum_{i=1}^{N} \tilde{u}_i = \tilde{u} - U$$

$$u' = \left(\frac{1}{N}\sum_{i=1}^{N} u_i^{\,2}\right)^{1/2}$$

Using these values, the turbulence intensity (Tu%) of the flow at a given point was calculated (assuming isotropic turbulence) by:

$$Tu\% = \frac{u'}{U}$$

The autocorrelation (R_v) of the fluctuating component of velocity (normalized such that R_v is equal to 1 at zero lag, τ=0), was calculated by:

$$R_v(\tau) = \left(\frac{\overline{u(t)\cdot u(t+\tau)}}{u'^2} \right) = \frac{1}{N} \left(\frac{\sum_{i=1}^{N} u_i \cdot u_{i+j}}{u'^2} \right) \quad \text{where} \quad \tau = j \cdot \Delta t$$

The autocorrelation was used to determine the integral time scale ($\Im$) by integrating under the curve to the first zero crossing.

$$\Im = \int_{t=0}^{\infty} R_v(\tau)d\tau = \sum_{i=1}^{N_0} R_{v_i} \cdot \Delta\tau$$

The streamwise integral length scale, which is representative of the largest eddies in the turbulent flowfield, was then determined by invoking Taylor's hypothesis of frozen turbulence:

$$\Lambda_x = U \cdot \Im$$

where N_0 is the point of the first zero crossing.

The probability density function (PDF) of each set of velocity data was also determined. The PDF is useful in visualizing the comparison of mean velocity and deviation of the data from the mean (proportional to Tu%) of different data sets. The PDF also demonstrates the Gaussian behavior of the data. The PDF of a data set was done by "binning" the velocity data into discrete bins (histogram) and normalizing by:

$$PDF = \frac{N_i}{N_{Total} \cdot \Delta\tilde{u}}$$

Finally, the power spectral density (PSD) each data set was determined by:

$$PSD = \frac{2 \cdot FFT(u) \cdot FFT^*(u)}{\Delta f} \quad \text{where * denotes the complex conjugate}$$

The power spectral density was frequency averaged to give a cleaner curve by averaging PSD data over a frequency range of Δf=100 Hz (data points over every 100 Hz were averaged to be a single point). The power spectral density gives an indication of turbulent energy content of the flow at different frequencies, which are inversely proportional to the size of the turbulent eddies in the flow (the wave number, κ, is equal to 2πf/U). For comparison, in the discussion section, the PSD data was normalized by:

$$\frac{U}{u'^2 \cdot \Lambda_x}$$

and compared to the Von Kármán spectrum equation:

$$\frac{E(f)\cdot U}{u'^2 \cdot \Lambda_x} = 4 \cdot \left(1 + \left(\frac{8\pi f \cdot \Lambda_x}{3 \cdot U}\right)^2\right)^{-5/6}$$

Using these statistical and spectral analysis tools, the characteristics of the turbulence could be determined.

Experimental Turbulence Data

This section uses the tools described to characterize the turbulence from the designed grid experiments both with and without active blowing. As discussed, four locations spaced in the streamwise direction were chosen to take hotwire measurements at mid-passage (3 inches from the sidewalls and 6 inches from the top and bottom walls). Mid passage is directly behind one of the blowing bars of the grid. Table 1 gives the axial location in bar widths (bars are 1 inch in width) downstream of the grid:

Location #	**Distance Downstream of Grid (Bar Widths)**
1	9.5
2	13.5
3	17.5
4	21.5

Table 1: Locations of Data Acquisition Points

The hotwire data at each of these points was reduced using a Matlab code to calculate statistics and autocorrelation to determine turbulence intensity and integral length scale. A sample of the Matlab code file written to accomplish all calculations in this report is included as Appendix A. The mean flow velocity, turbulence intensity, and integral length scale at each location for different blowing rates from the bars (including no blowing) are shown in Figure 4 through Figure 6, respectively. In the absence of a system of measuring plenum pressure independently for each bar, the blowing rate was estimated by how far the upstream ball valves between the blowing air plenum and grid bars were opened. There is some run-to-run error inherent in this method.

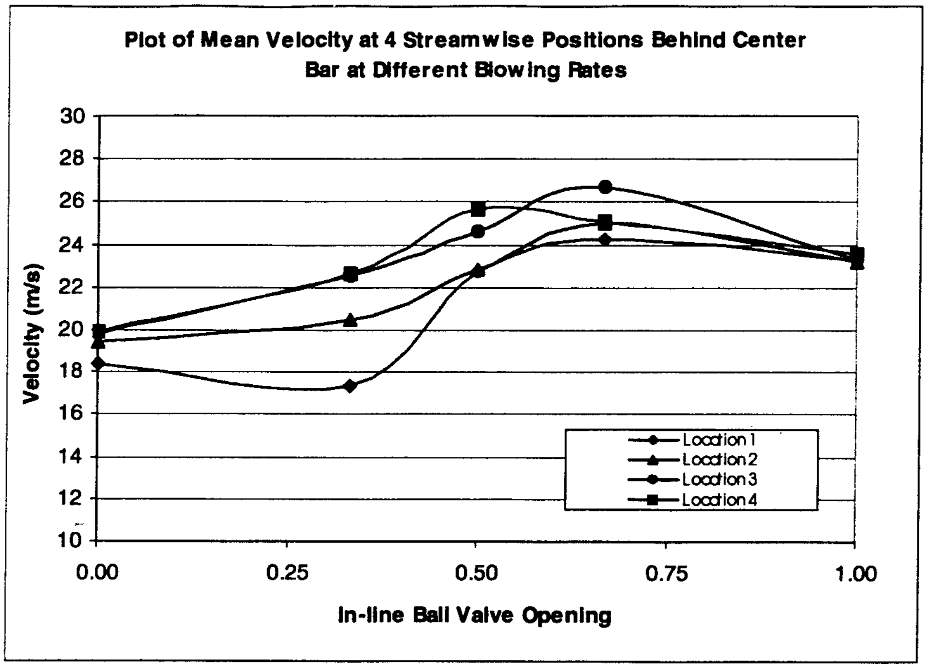

Figure 4. Plot of Mean Velocity at 4 Streamwise Locations at Different Blowing Rates

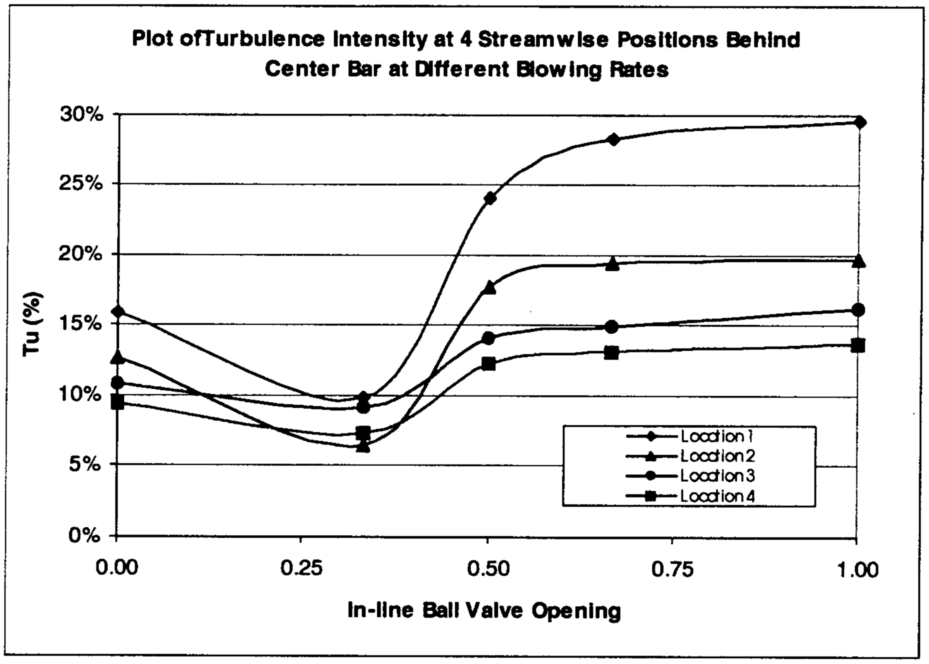

Figure 5. Plot of Turbulence Intensity at 4 Streamwise Locations at Different Blowing Rates

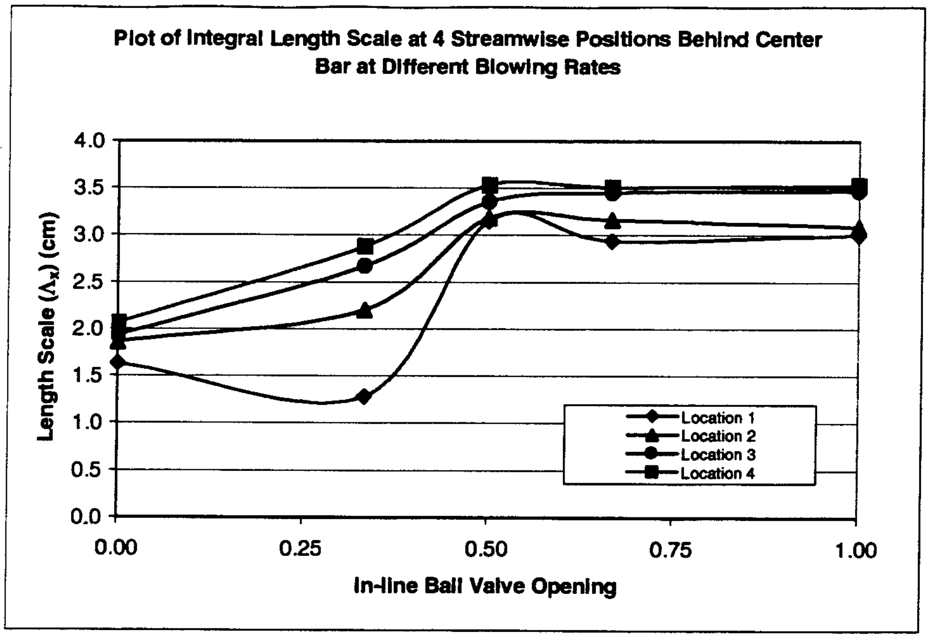

Figure 6. Plot of Integral Length Scale at 4 Streamwise Locations at Different Blowing Rates

The mean flow in the test section without the grid installed was approximately 20 m/s at center passage, which is independent of streamwise measurement location. Figure 4 demonstrates that at locations near the grid without blowing, there is a velocity deficit due to the wake of the grid bars. This velocity deficit decreases as you march in the streamwise direction and away from the influence of the wake. The general trend in velocity with blowing is that the velocity at each location increases with increased blowing as the bar wake is filled in with higher momentum fluid and eventually a jet forms. The initial decrease in mean velocity at the lowest blowing rate at Location 1 could not be explained. The decrease in mean velocity at the highest blowing rate is due to the plenum pressure dropping, most likely due to the inlet flow to the plenum choking. The turbulence intensity of the flow without the grid installed was approximately 2%. Figure 5 demonstrates that with the grid in place without blowing, the intensity increases significantly to approximately 10-15% depending on streamwise location. As blowing is activated and increased, there is first a decrease in turbulence intensity, then a steady increase with blowing rate. The initial decrease is probably due to filling in the wake of the bars, which essentially reduces the effectiveness (or effective bar width) of the grid. The integral length scale of the flow was shown, with the exception of one point, to steadily increase with blowing rate as can be seen in Figure 6. The length scale at higher blowing rates is seen to "settle out" with no further increase. For the data presented here, the blowing rate (blowing plenum pressure) is just an initial setting. The current results show that at approximately 18 bar widths downstream of the grid, the turbulence intensity is as high as 17% with an integral length scale of 3.5 cm. Continuing work is being done by myself to determine the optimal plenum pressure and internal bar pressure that will provide the desired turbulence intensity and length scale at 18 bar widths downstream of the grid, as well as investigate the uniformity of the flow from the blown grid in the cross-stream direction.

Statistics and Power Spectra

At each measurement location, the PDF, autocorrelation and PSD were determined and the results compared for each blowing rate. Figure 7 through Figure 9 present the PDFs, autocorrelations, and PSDs at each location for varying blowing rates, respectively.

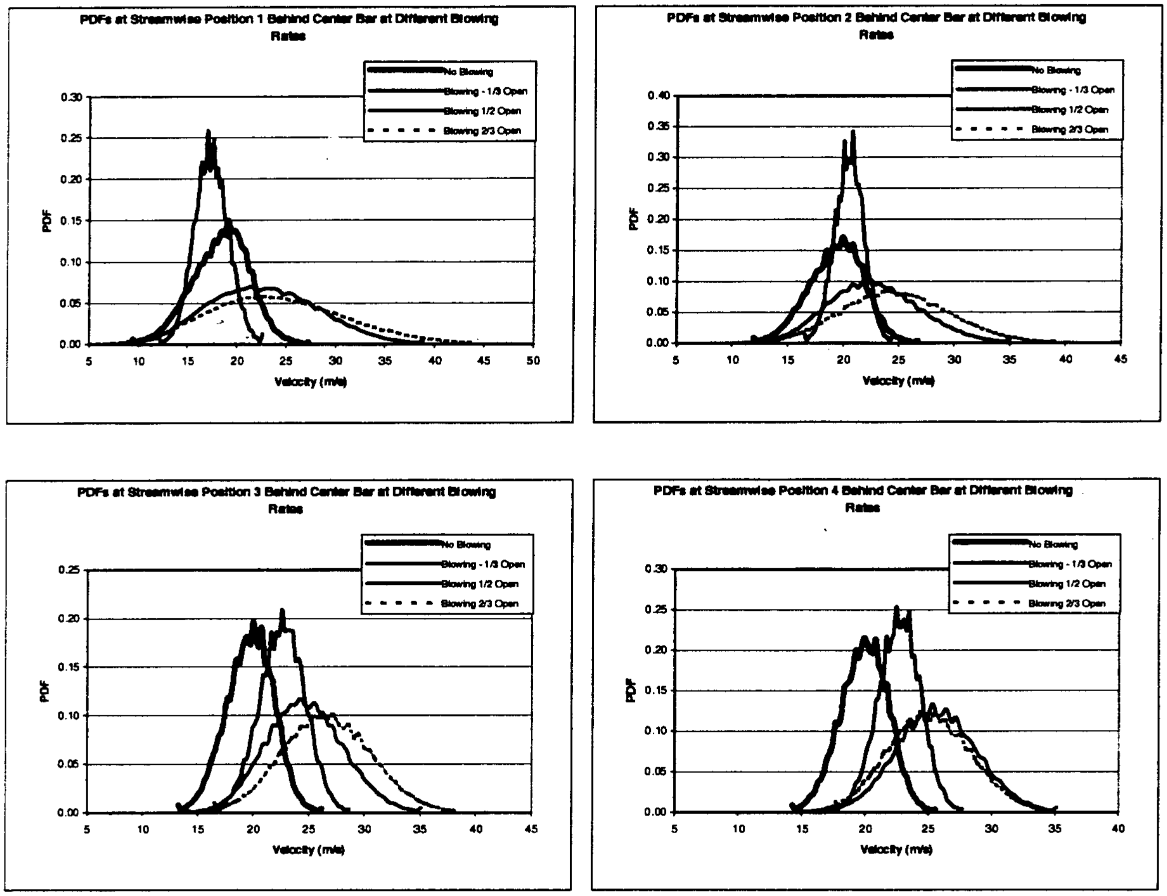

Figure 7. Probability Density Functions (PDF) at Each Streamwise Measurement Location at Different Blowing Rates

The probability density functions at different blowing rates for each measurement location (Figure 7) demonstrate that as blowing is increased, the mean velocity and deviation from the mean (which is proportional to the turbulence intensity) change in the manner discussed in the previous section. With the exception of one point at Location 1, the mean velocity tends to increase and the turbulence intensity ("thickness" of the PDF) tends to increase as the blowing rate is increased. The PDFs demonstrate the Gaussian behavior of the velocity data.

Through observation of the autocorrelation curves (Figure 8), it can be seen that the first zero crossing value does not change significantly with increased blowing at each streamwise location. However, the shape of the curves changes with increased blowing, so integrating under the curve to obtain the integral time scale will yield increasing time scales with increasing blowing rate. This fact, coupled with the mean velocity change will, in general, cause a corresponding increase in length scale with increasing blowing rate. This is in agreement with the results shown in Figure 6.

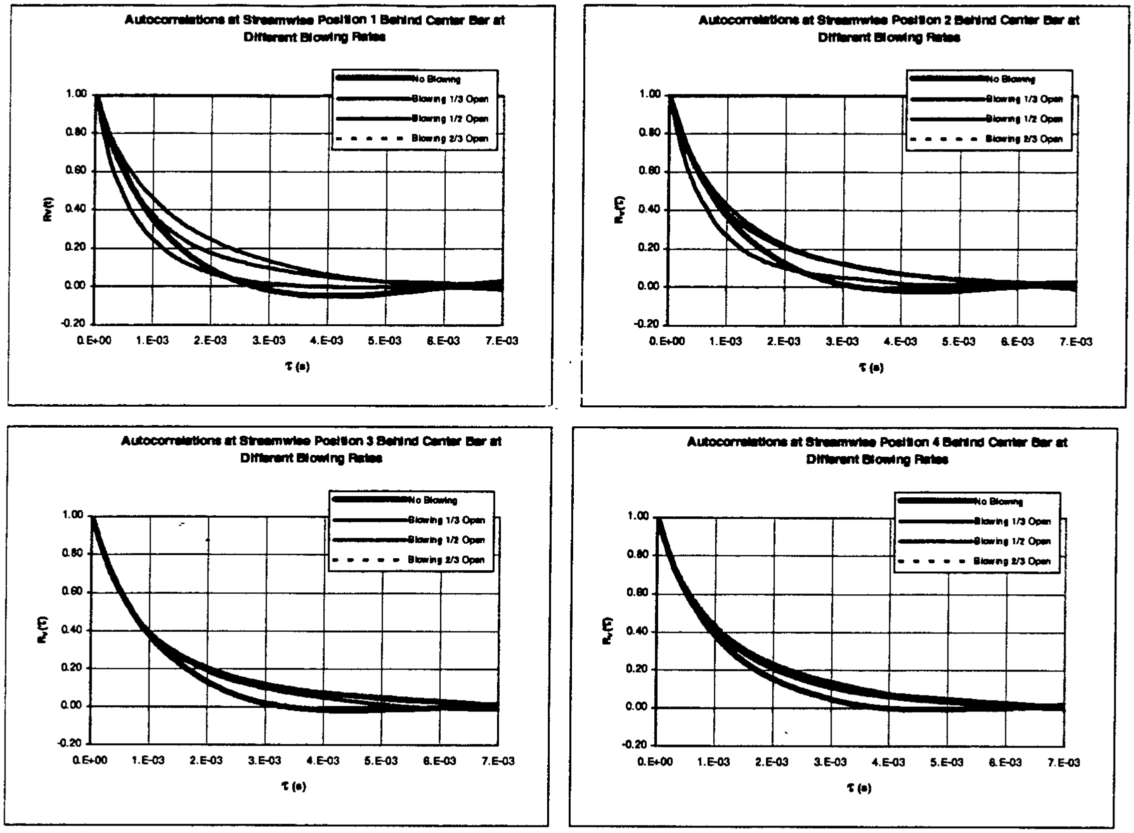

Figure 8. Autocorrelations (R_v) at Each Streamwise Measurement Location at Different Blowing Rates

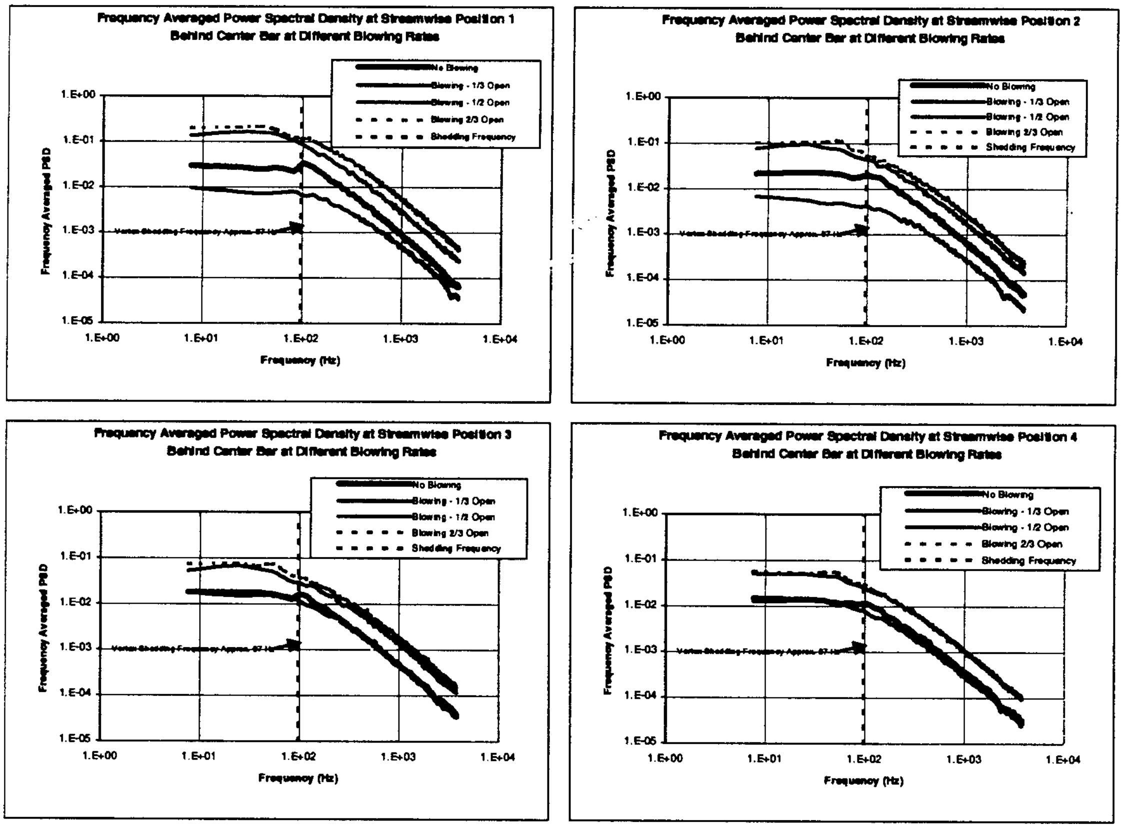

Figure 9. Power Spectral Density (PSD) at Each Streamwise Measurement Location at Different Blowing Rates

The power spectral density (PSD) plots for each location confirm the results for the turbulence intensity. As mentioned earlier, power spectral density gives an indication of turbulent energy content of the flow at different frequencies, which is inversely proportional to the size of the eddies. The PSD plots for each location at different blowing rates (Figure 9) demonstrate that as blowing is increased the turbulent energy at each frequency (or wave number) increases. Integrating under the PSD will yield the RMS of the velocity fluctuations (u'), which is proportional to turbulence intensity. At each location, the PSD without blowing can be seen to have a "hump" around 100 Hz. This is believed to be a product of weak vortex shedding from the bars without blowing. This phenomenon, and a more detailed analysis of the PSD for select data sets; will be discussed in detail in the discussion section.

Discussion

Comparison to Grid Generated Turbulence

The set of tests performed involved collecting data at four streamwise positions to compare the published data to grid generated turbulence studies. The "grid" in this work is actually a series of horizontal bars rather than a 2-D grid arrangement, however, it is suggested that the data should still match well with grid generated turbulence correlations. Studies performed by Roach[6] and Baines and Peterson[7] demonstrated the streamwise variation of turbulence intensity and integral length scale behind tube bundles and screens. From these studies, it has been shown that the turbulence decay and length scale dispersion can be characterized by equations in the form:

$$Tu\% = c \cdot \left(\frac{x}{d}\right)^{n} \quad \text{and} \quad \Lambda_x = a \cdot d \cdot \left(\frac{x}{d}\right)^{m}$$

where c and a are constants given as 0.80 and 0.20, respectively, x is the streamwise distance, d is the bar width, and n and m are exponents. The value of n is typically –5/7 and m is between 0.5 and 0.56 according to the published data. The data collected behind the grid in this work was compared to the published curves. Figure 10 through Figure 12 show the mean velocity, turbulence intensity, and integral length scale versus streamwise measurement location both with and without blowing. One blowing rate was chosen for simplicity, the "valve half open" condition. From Figure 10, it can be seen that without blowing, the velocity data increases slightly as you march downstream and get out of the influence of the bar wake, as discussed earlier. The same type of trend is seen for the velocity with blowing, however, the velocity increases much faster as a result of the blowing filling in the wake. The streamwise decay of turbulence intensity is shown in Figure 11. The data with and without blowing is plotted along with the turbulence decay equation given by Roach and Baines and Peterson. Similarly, the streamwise dispersion of turbulent length scale is shown in Figure 12. These two figures demonstrate that blowing follows a different "decay law" than grid generated turbulence. The decay of turbulence intensity without blowing agrees well with the correlations, however the integral length scale does not agree as well. Deviation from the correlations could be due to the geometry used here (i.e. horizontal square bars versus round wire mesh grids). It is also possible that the discrepancy is due to a contraction being present downstream of the grid. The turbulence intensity data with blowing was shown to obey a power law of $Tu\%=1.5(x/d)^{0.714}$, however this was only valid at this blowing rate. Increasing or decreasing blowing rate changed this relationship.

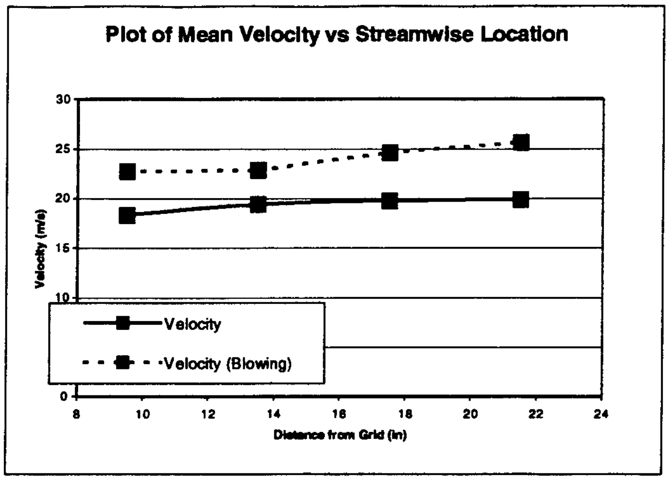

Figure 10. Variation of Mean Velocity in the Streamwise Direction with and without Blowing

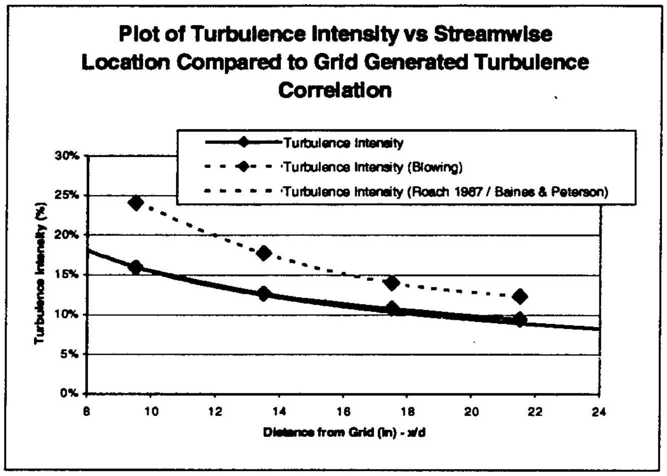

Figure 11. Variation Turbulence Intensity in the Streamwise Direction with and without Blowing

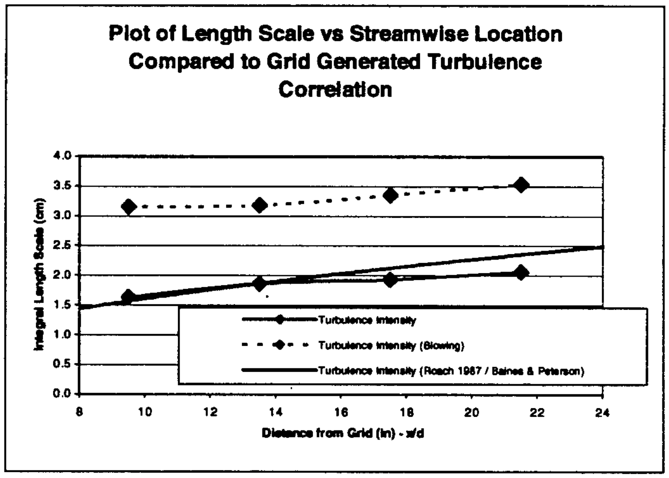

Figure 12. Variation Length Scale in the Streamwise Direction with and without Blowing

The probability density function of the data with and without blowing, shown in Figure 13 demonstrate, as before, the increase in the mean velocity and turbulence intensity in the streamwise direction. Again, it can be seen from the PDFs that as we march along in the streamwise direction, the mean velocity increases and the deviation becomes smaller, indicating a decrease in turbulence intensity. The relative widths at each location with and without blowing indicate that the turbulence intensity is higher for the blowing case and the mean increases more with blowing since the velocity deficit is overcome earlier due to the jets filling in the wake behind the bars. Of interest, and as yet unexplained, is that the PDFs for the unblown cases (and in the blown cases to a lesser extent) collapse down to a common curve on the high side (+3σ) of the mean velocity.

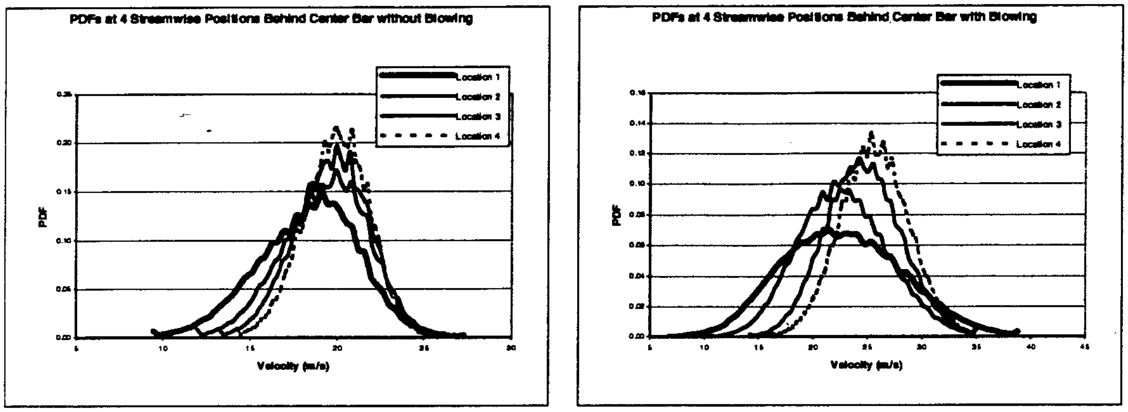

Figure 13. Probability Density Functions of Velocity for Various Streamwise Positions with and without Blowing

Determination of Vortex Shedding for Unblown Grid

In the results presented in the spectra for the velocity data, it was indicated that the spectra for the unblown grid data displayed a "hump" in the data around 100 Hz. The possibility of vortex shedding occurring from the bars was investigated. The vortex shedding frequency of a body can be described by the dimensionless parameter of Strouhal (S),

$$S = \frac{f_s \cdot D}{U}$$

where f_s is the vortex shedding frequency, D is the width of the bar, and U is the mean velocity upstream of the bar. The Strouhal number is a function of the geometry of the body and Reynolds number. For a square bar in cross-flow, the Strouhal number has been demonstrated[10,11] to be 0.13 (versus 0.21 for circular cylinders) with strongest vortex shedding in the range of $Re_D \sim 10^5$. Using a value of S=0.13, a mean velocity of 19 m/s upstream of the bar and a diameter of 1 inch (0.0254 m), the shedding frequency was determined to be 97 Hz. Figure 14 shows the power spectral density at each streamwise location without blowing. It can be seen from the plot that the "hump" in the PSD is centered on approximately 100 Hz. The magnitude decreases with streamwise distance, suggesting that the vortex shedding is relatively weak and the vortices break up as the flow progresses downstream. This makes sense, since the Reynolds number based on the diameter of the bar is only Re_D=32,000, whereas according to the literature, vortex shedding for square bars occurs at a $Re_D \sim 10^5$. Therefore, we would not expect strong vortex shedding from the bars in this velocity regime. However, this is of importance in continuing work, as vortex shedding from the bars in the transonic facility, where the velocity at the bars can be as high as 120 m/s may result in stronger vortex shedding. Blowing should eliminate concerns with vortex shedding, but this analysis is worth consideration in the transonic tunnel.

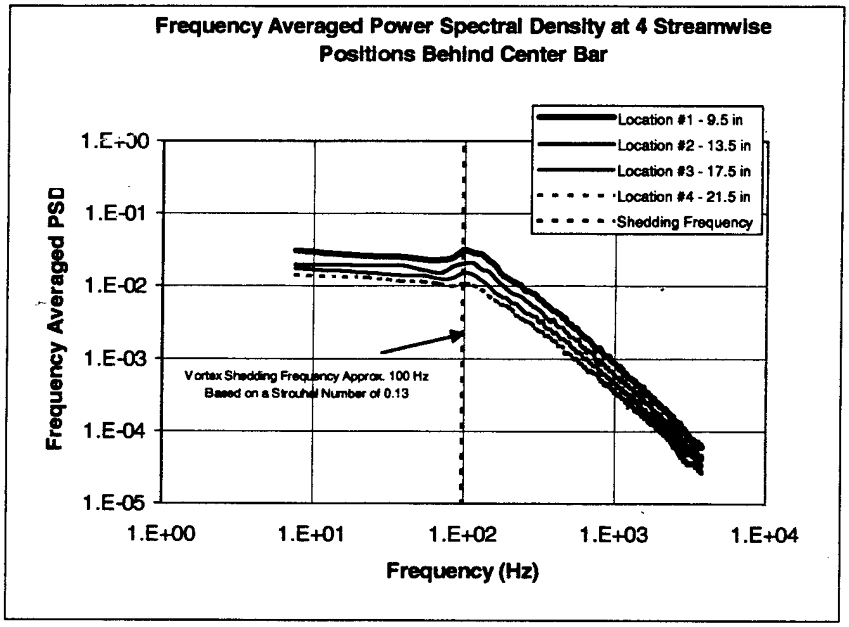

Figure 14. Power Spectra at Each Measurement Location without Blowing

Comparison of Power Spectral Density of Turbulent Flow with Von Kármán Spectra

For purely isotropic turbulence in the absence of outside forces and viscous dissipation, the Von Kármán spectrum equation holds:

$$\frac{E(f)\cdot U}{u'^2\cdot\Lambda_x}=4\cdot\left(1+\left(\frac{8\pi f\cdot\Lambda_x}{3\cdot U}\right)^2\right)^{-5/6}$$

where E(f) is the power spectral density. If the PSD for the velocity data is normalized by:

$$\frac{U}{u'^2\cdot\Lambda_x}\quad\text{and plotted versus}\quad\frac{2\pi f\cdot\Lambda_x}{U}=\kappa\cdot\Lambda_x\quad\text{where } \kappa \text{ is the wave number}$$

the results can be directly compared to the Von Kármán spectrum equation.

Figure 15 and Figure 16 are comparisons of two PSDs (one with blowing and one without blowing 20 bar widths downstream of the grid) from this study with the Von Kármán equation. There are three regions of note in the PSD. The first region is the relatively flat region at the low wave numbers at the beginning of the curve, which contains the relatively low energy, large length scale turbulent eddies. At the end of this region is where the most energetic eddies exist, which occurs where $\kappa\cdot\Lambda_x\approx1$ (i.e. the wave number is approximately equal to the inverse of the integral length scale). This wave number is denoted as κ_e. Through observation of a plot of the wave number and normalized power spectra product (shown in Figure 17 and Figure 18), it can be seen from the spectra that the most energetic scales should occur at $\kappa \cdot \Lambda_x \approx 1$. The data with blowing match up fairly well with the Von Kármán curves, however, an interesting point to note is that in both Figure 15 and Figure 17 (data for grid without blowing), there is a slight departure of the data from the theoretical Von Kármán curves. This is believed to be due to the vortex shedding discussed earlier. In Figure 17, using the previously calculated vortex shedding frequency of 97 Hz, and for the case plotted in the figures, U was equal to 19.91 m/s and Λ_x was equal to 2.06 cm, yields $\kappa \cdot \Lambda_x = 0.778$. This line is shown in both plots. This is close to $\kappa \cdot \Lambda_x \approx 1$, but as can be seen, there is a much higher peak in the PSD of the unblown grid compared to the Von Kármán curve. It is possible that coherent vortex shedding structures are still in existence 20 bar widths downstream of the grid, although they do not seem to be very strong.

The next region is a region where the spectrum follows a $\kappa^{-5/3}$ power law decay. This region is also called the inertial subrange and is the region where the higher frequency (smaller scale) turbulence exists independently of larger scales and energy is cascaded down from large scales to small scales until the eddies are sufficiently small enough to be in the range of viscous dissipation. This region is useful in determination of the dissipation rate, ε, of the turbulence. By curve-fitting the data in the inertial subrange to an equation of the form $E(\kappa)=A \cdot \varepsilon^{2/3}\ k^{-5/3}$, the dissipation rate can be determined. The value of A varies depending on the source, with values of 0.50-0.53 being reported[12,13]. The dissipation rate was not calculated for this work. The third region is the departure from the –5/3 decay law and is a product of viscous dissipation and occurs at very small scales (Kolmogorav or dissipation length scales). This region is readily evident in both the unblown and blown grid data. The inertial subrange of the blown grid seems to be much larger than that of the unblown grid, as the data for the blown grid holds to the Von Kármán curve and –5/3 slope for a larger range of wave numbers.

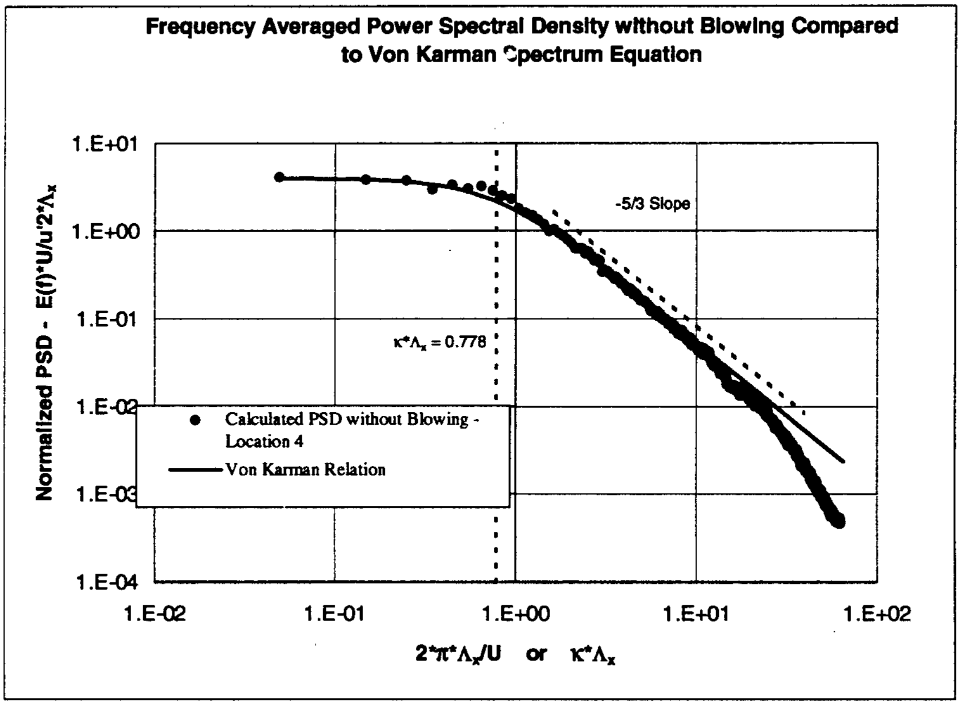

Figure 15. PSD Data without Blowing Compared to Von Kármán Relation

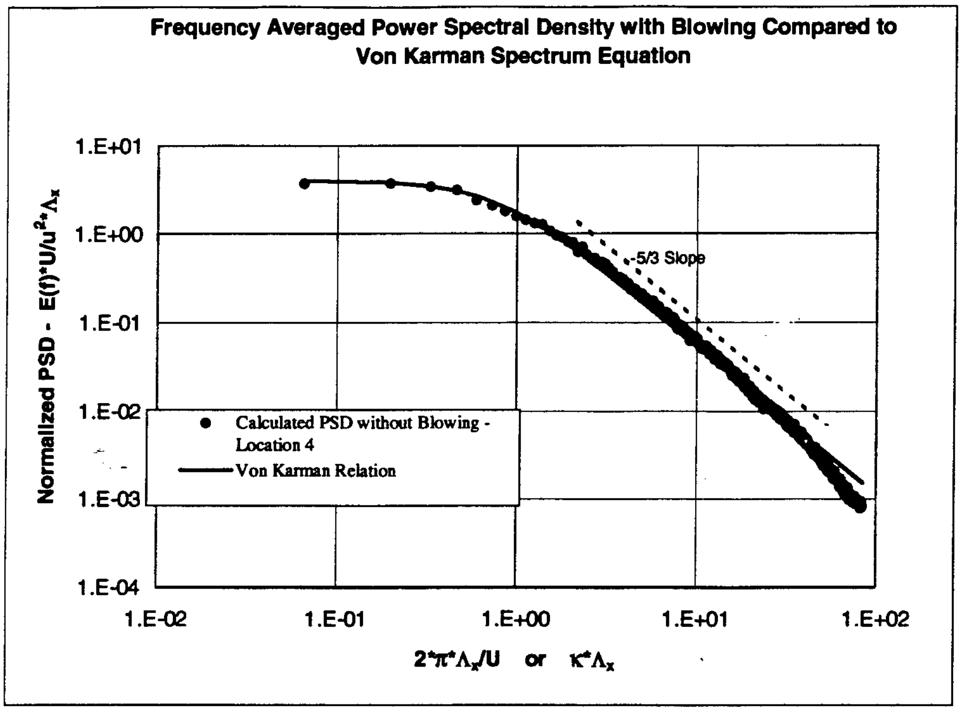

Figure 16. PSD Data with Blowing Compared to Von Kármán Relation

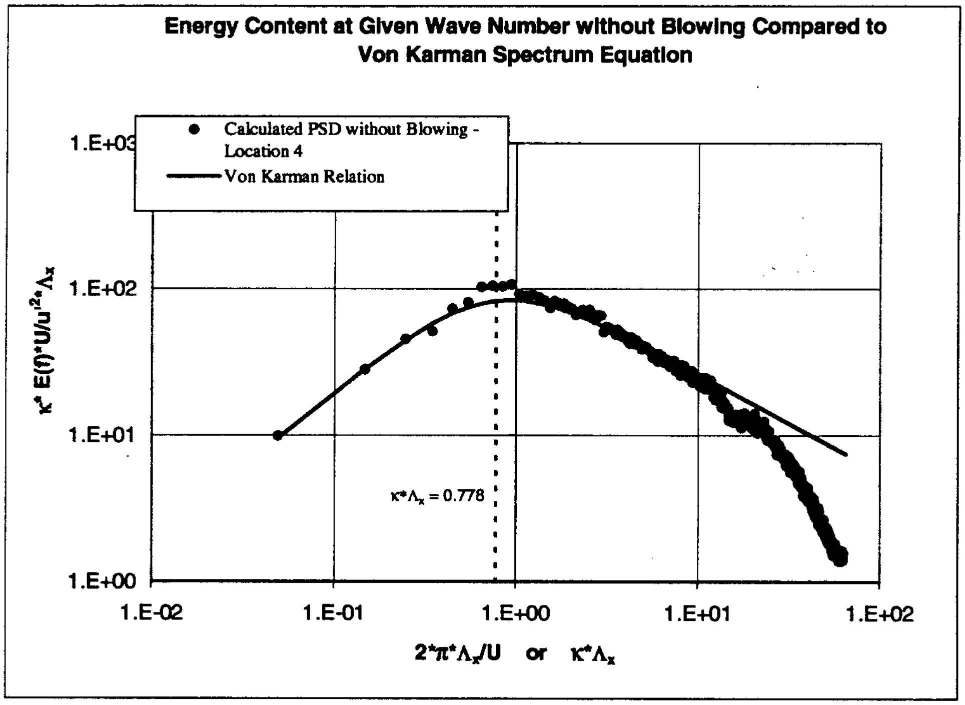

Figure 17. Energy Content versus Wave Number without Blowing Compared to Von Kármán Relation

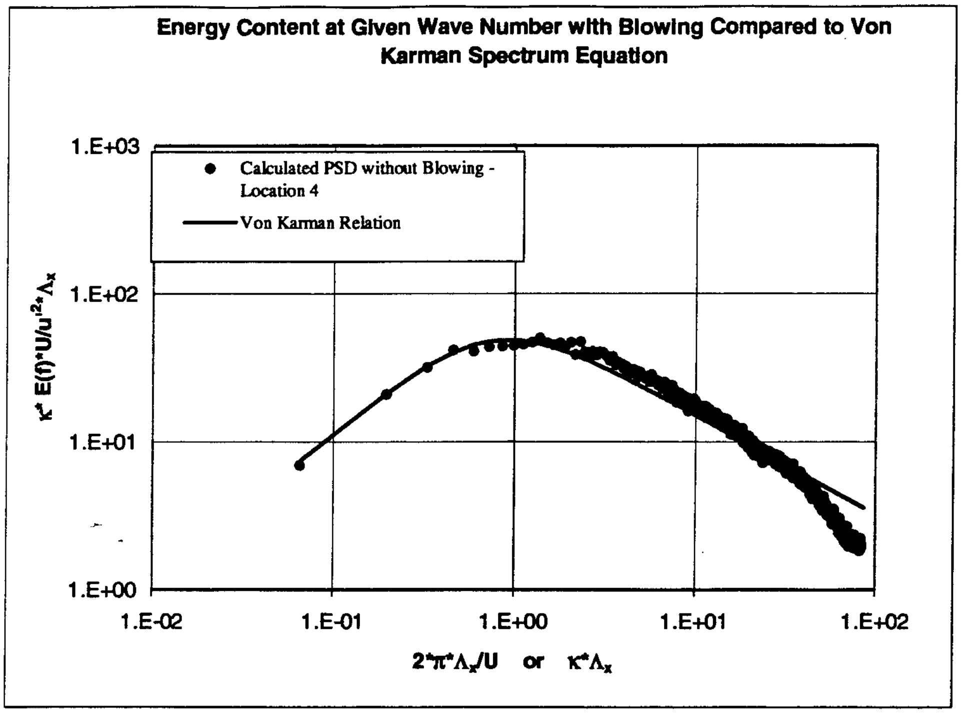

Figure 18. Energy Content versus Wave Number with Blowing Compared to Von Kármán Relation

The wave number, κ_d, where viscous dissipation starts can be related to the Kolmogorav length scale (η) by:

$$\kappa_d \cong \frac{0.1}{\eta}$$

The value of κ_d can be estimated by plotting the dissipation energy spectrum $\kappa^2 \cdot E(f)$. Figure 19 shows the dissipation spectrum both with and without blowing. The value of κ_d is defined as the maximum of these curves, where the derivative of the dissipation spectrum with respect to wave number is zero. From comparison of the curves, it is not readily apparent which has a higher κ_d. However, these curves do provide some insight as to the relative size of the Kolmogorav length scale, within the limitations of the measurement technique. Assuming (from Figure 18) that κ_d is approximately 1000, this would yield a Kolmogorav length scale of $\approx 10^{-4}$ m. The relative size of the Kolmogorav length scale to the integral length scale is on the order of 100 times (the Kolmogorav length scale is 100 times smaller than the integral length scale). This can be checked by using a relation of the small length scales (Kolmogorav) to large length scale (integral length scale):

$$\frac{l}{L} = \mathrm{Re}_L^{-1/2} \quad \text{or} \quad \frac{\eta}{\Lambda_x} = \mathrm{Re}_{\Lambda_x}^{-1/2} = \left[\frac{\nu}{U \cdot \Lambda_x}\right]^{-1/2}$$

For the flow in this work, the mean velocity, U, is approximately 20 m/s, ν is approximately 20 $\times 10^{-6}$ m^2/s and Λ_x is 2-3 cm (depending on whether blowing is initiated). Using these estimated values, the value of $\mathrm{Re}^{-1/2}$ suggests that the Kolmogorav length scale (η) is approximately 140 times smaller than the integral length scale (Λ_x), which is in good agreement with the value determined using the dissipation wave number.

For the data taken in this work, a hotwire probe of length is about 1mm. The Kolmogorav length scales we estimated to be approximately 10^{-4} m, which is 10 times smaller than the length of the hotwire. From this analysis, with the current limitations on the length of hotwire probes, the probe cannot be expected to measure length scales in the Kolmogorav scale range.

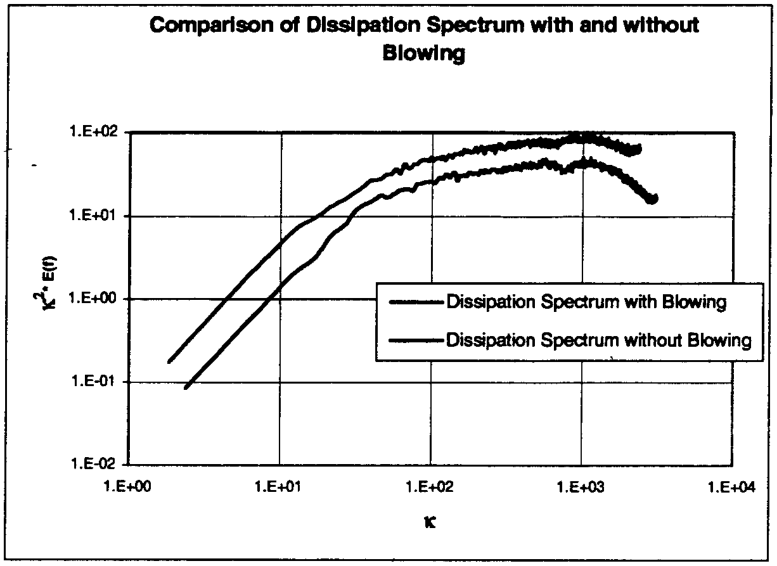

Figure 19. Comparison of Dissipation Spectrum with and without Grid Blowing

Conclusions

The results of initial testing of an actively blown grid for generation of large length-scale, high intensity freestream turbulence have been reported. The preliminary testing of the grid showed that at the current blowing rates (blowing plenum pressure of 60 psig), the grid could achieve a turbulence intensity,Tu%, of 17% and an integral length scale, Λ_x, of 3.5 cm. The desired intensity and length scale from this grid are approximately 20% and 4 cm, respectively. Continuing work will optimize the blowing rate and investigate the uniformity of the flow in the cross-stream direction with blowing. Also presented were statistical and spectral analysis tools to fully characterize the turbulence generated by the grid, both with and without active blowing. From these analyses, the decay of turbulence intensity and length scale in the streamwise direction were presented and compared to published correlations for decay of turbulence and dispersion of length scale. The current data without blowing agree well with the turbulent decay correlations, but there is some discrepancy between the measured length scale dispersion and the published correlations. This discrepancy will be investigated in further work. The blown grid data seem to follow a different decay law, which varies with blowing rate.

Spectral analysis of the data demonstrated that the blown grid power spectral density and energy content at different wave numbers agrees well with the Von Kármán spectrum equations, which are the theoretical energy spectrum for purely isotropic turbulence in the absence of outside forces and viscous dissipation. The data for the unblown grid was shown to deviate slightly from the Von Kármán spectrum in the region prior to the inertial subrange. It was shown that the unblown grid data contains additional energy in a small frequency range corresponding to a frequency where vortex shedding can be expected from the bars. This vortex shedding was demonstrated to be relatively weak and was shown to decay as the flow progressed in the streamwise direction. The blown grid data was also shown to have a larger inertial subrange than the grid data without blowing.

Finally, an attempt was made at determining the dissipation (Kolmogorav) length scale. Through analysis of the dissipation energy spectra of the data, the dissipation wave number was estimated. With the data collected, it was difficult to discern a difference between the dissipation scale between the blown and unblown data. The dissipative length scales were estimated within the limitations of the measurement technique to be on the order of 100 times smaller than the integral length scale, which is the most energetic scale.

References

1. Sauer, J. (1996), "The SUDI Turbulence Generator – A Method to Generate High Freestream Turbulence Levels and a Range of Length Scales," Thesis, University of Wisconsin/Universitat Karlsruhe.

2. Radomsky, R.W. and Thole K.A. (1998), "Effects of High Freestream Turbulence Levels and Length Scales on Stator Vane Heat Transfer," ASME Paper 98-GT-236.

3. Giel, P.W., Bunker, R.S., Van Fossen, G.J. and Boyle, R.J. (2000), "Heat Transfer Measurements and Predictions on a Power Generation Gas Turbine Blade," ASME Paper 2000-GT-0209.

4. Boyle, R. J., Lucci, B.L., Verhoff, V.G., Camperchioli, W.P. and La, H. (1998), "Aerodynamics of a Transitioning Turbine Stator Over a Range of Reynolds Numbers," ASME Paper 98-GT-295 (NASA/TM-1998-208408).

5. Mehendale, A.B. and Han, J.C. (1992), "Influence of High Mainstream Turbulence on Leading Edge Film Cooling Heat Transfer," ASME Journal of Turbomachinery, Vol. 114, pp. 707-715.

6. Roach, P.E. (1987), "The Generation of Nearly Isotropic Turbulence Downstream of Streamwise Tube Bundles," Int. Journal of Heat & Fluid Flow, Vol. 114, pp. 117-125.

7. Baines, W.D. and Peterson, E.G. (1951), "An Investigation of Flow Through Screens," Trans. of the ASME, July 1951, pp. 467-480.

8. Personal Communication with Dr. Jim Van Fossen, NASA Glenn Research Center. Research paper to be published in 2000/2001.

9. I have this paper, but could not locate it. I believe it is by Moss and Oldfield at Oxford.

10. Blevins, R.D., Flow-Induced Vibration 2nd Ed., Krieger Publishing, 1994.

11. Bearman, P.W. et al.(1987), "Experiments on Flow-Induced Vibration of a Square Section Cylinder," Journal of Fluids and Structures, Vol 1., 1987, pp. 19-34.

12. Libby, P.A., Introduction to Turbulence, Taylor and Francis, Washington D.C., 1996.

13. Hinze, J.O., Turbulence, McGraw-Hill, New York, 2nd Edition 1987.

AN INVESTIGATION OF HEAT TRANSFER IN A FILM COOLED TRANSONIC TURBINE CASCADE, PART I: STEADY HEAT TRANSFER

D. E. Smith, J. V. Bubb, O. Popp, H. Grabowski III, T.E. Diller, J.A. Schetz, W.F. Ng
Virginia Polytechnic Institute and State University
Blacksburg, VA 24061

ABSTRACT

Experiments were performed in a transonic cascade wind tunnel to investigate the film effectiveness and heat transfer coefficient on the suction side of a high-turning turbine rotor blade. The coolant scheme consisted of six rows of staggered, discrete cooling holes on and near the leading edge of the blade in a showerhead configuration. Air was cooled in order to match the density ratios found under engine conditions. Six high-frequency heat flux gauges were installed downstream of the cooling holes on the suction side of the blade. Experiments were performed with and without film and the coolant to freestream total pressure ratio was varied from 1.02 to 1.19. In order to simulate real engine flow conditions, the exit Mach number was set to 1.2 and the exit Reynolds number was set to 5×10^6. The freestream turbulence was approximately 1%. The heat transfer coefficient was found to increase with the addition of film cooling an average of 14% overall and to a maximum of 26% at the first gauge location. The average film cooling effectiveness over the gauge locations was 25%. Both the heat transfer coefficient and the film cooling effectiveness were found to have only a weak dependence upon the coolant to freestream total pressure ratio at the gauge locations used in this study.

NOMENCLATURE

B	blowing ratio $(\rho u)_c/(\rho u)_f$
d	cooling hole diameter (1 mm)
C	specific heat of air, 1005 J/(kg K)
h	heat transfer coefficient w/o film cooling
h_c	heat transfer coefficient w/ film cooling
I	momentum flux ratio $(\rho u^2)_c/(\rho u^2)_f$
M	density ratio ρ_c/ρ_f
p	static pressure
Pr	Prandtl Number, 0.71
q	heat flux
r	recovery factor
T_{aw}	local adiabatic wall temperature
T_c	coolant exit temperature
T_d	T_t-T_r
T_r	local recovery temperature
T_t	freestream total temperature
T_w	local wall or blade temperature
u	local freestream velocity
η	film effectiveness

Subscripts

$_c$	coolant or w/ film cooling
$_f$	freestream

INTRODUCTION

The efficiency of a gas turbine engine increases with turbine inlet temperature. In the ongoing effort to raise the turbine inlet temperature the gas stream temperature is made to greatly exceed the operating temperatures of blade materials, requiring elaborate blade cooling techniques to be developed. One such cooling scheme is film cooling, in which cool air drawn from the compressor is forced through holes on the surface of the turbine blade in order to insulate the blade from the hot engine environment. Since this air is seen as a loss of work for the engine, it is necessary for the thermal designer to gain an understanding of the physics of film cooling and the parameters that affect it in order to minimize the air drawn from the compressor.

In an attempt to provide information about the heat transfer to film cooled turbine blades, many flat plate experiments have been performed. These experiments allowed researchers to amass a great deal of information about the parameters that affect heat transfer into a film cooled surface. A compilation of early experimental work done on flat plates is given by Goldstein (1971).

Schwarz et al. (1990) investigated the effects of curvature and blowing ratio on the film cooling effectiveness of a convex surface. They found that curved surfaces had better film cooling effectiveness than flat plates. Also, Schwarz et al. found that at low blowing rates, film cooling is more effective on the suction side of the blade than on the pressure side. This work was an intermediate step between flat plates and investigations of heat transfer into realistic blade geometries.

Horton et al. (1985) investigated film cooling heat transfer of a realistic turbine blade profile mounted in a linear cascade. Thin-film resistance sensors were used in a short duration blow down tunnel to capture the transient surface temperature history. Horton et al. were able to obtain measurements of the heat transfer coefficient at several locations along both the pressure and suction sides of the blade.

Researchers at G. E. Aircraft Engines performed heat transfer measurements on a heavily film cooled inlet nozzle guide vane (NGV) in a linear cascade with realistic flow conditions (Abuaf et al., 1997). Thermocouples embedded in a thin-walled turbine blade were used to measure the transient surface temperature. Heat transfer coefficient and effectiveness profiles were obtained for both sides of the blade. Experimental results showed that the heat transfer coefficient increased as film cooling was added.

The effects of freestream turbulence on the heat transfer into a film cooled turbine blade were investigated by Ekkad et al. (1995). Thermochromic liquid crystals (TLC's) were used to obtain the transient surface temperature history. A general conclusion was shown that high freestream turbulence results in an increased heat transfer coefficient and a slightly reduced film cooling effectiveness.

Researchers at Oxford University used thin-film gauges to study the heat transfer into a heavily film cooled NGV (Guo et al., 1996 and 1997). Their measurements were performed in an annular cascade with attempts made to simulate realistic engine conditions. A mixture of SF_6 and Argon was used as a coolant. The heat transfer coefficient and film cooling effectiveness profiles were determined for the pressure side of the NGV.

In 1998, Drost et al. used TLC's to record the transient surface temperature history of an NGV airfoil exposed to a step input in heat transfer while in a linear cascade. They used a foreign gas as a coolant to obtain a realistic density ratio. They concluded that the film cooling effectiveness was higher near the cooling holes and that the mainstream turbulence level had a weak effect on suction side effectiveness, but that it increased suction side heat transfer coefficients.

The Virginia Tech facility consists of a transonic linear cascade of first stage turbine blades with a shower head film cooling scheme. Preliminary work on the same blade and cooling scheme with only a single gauge location was presented by (Popp et al., 1999). Measurements were made using thin-film heat flux gauges of both the heat transfer coefficient and film cooling effectiveness at six locations along the blade suction side surface. In the present paper, measurements along the length of the chord were made, and the influence of blowing parameters on the heat transfer coefficient and film cooling effectiveness is presented. Part II of this research presents the unsteady effects of shocks.

EXPERIMENTAL APPARATUS

Transonic Wind Tunnel

The experiments described in this paper were all performed in the Virginia Tech transonic wind tunnel, an intermittent blow down facility with an open discharge. A reciprocating compressor is used to load a high-pressure tank that serves as the supply for the mainstream flow. When released, air flows at a rate of approximately 10 kg/s through the system of pipes shown in Fig. 1. A fast-acting control valve is used to maintain the tunnel's total pressure at a constant value that was experimentally determined to give the desired exit Mach number. The pressure is constantly monitored and controlled by a pressure transducer upstream of the test section. The Virginia Tech wind tunnel also has the capacity for heated flows by utilizing the lower loop shown in Fig. 1. In the bottom of the loop there are two 36 kW resistance heaters which heat the air. This heated air is then circulated over a bank of copper tubes in the top of the loop by a small fan. The heated copper tubes act as a passive heat exchanger and heat the tunnel's mainstream flow during a run. During the course of a tunnel run the mainstream flow temperature drops, and as will be described later, this allows a range of density ratios over which the heat transfer coefficient and film cooling effectiveness is determined.

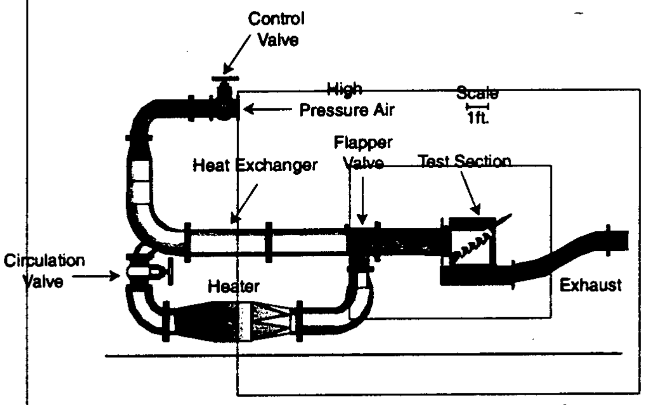

Figure 1: Transonic Wind Tunnel Facility

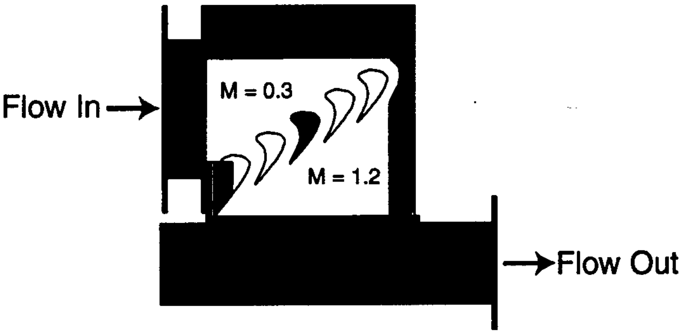

Figure 2: Schematic of Cascade Test Section

Cascade Test Section

The test section used to mount the rotor blades was constructed of aluminum with clear-acrylic side walls. The side walls give optical access to the flow in the passages and allow shadowgraph and Schlieren photography to be performed. A cut-a-way of the test section can be seen in Fig. 2. The test section contains four full blades and two half blades, a total of five flow passages. Flow enters the test section at Mach 0.3, is turned 128° while passing over the blades, and exits the test section at Mach 1.2. The shaded blade was instrumented and used to acquire all of the data presented in this paper. Schlieren imaging was used to demonstrate flow periodicity in the two passages around the instrumented blade.

Turbine Blade Design

The blade profile used in this study was a generic design given by GE Aircraft Engines and was made from aluminum. Measured and predicted Mach number profiles matched well for this blade design and were presented by Hale et al. (1997). The Reynolds number based on aerodynamic chord (13.6 cm) and unheated exit conditions is about $6x10^6$. The maximum value of the acceleration factor in the region of the sensors was approximately $1.2x10^{-6}$. Six rows of cooling holes are located near the leading edge in a showerhead arrangement, as can be seen in Fig. 3. All of the holes have a diameter of 1 mm and the spacing between holes is approximately 9.1 hole diameters. The four rows of cooling holes nearest the leading edge are all aligned normal to the streamwise tangent and are inclined at an angle of 30° to the surface where they emerge. The two rows of coolant holes farthest from the leading edge are both aligned parallel to the streamwise tangent. The gill holes on the suction side are inclined at an angle of 30° to the surface where they emerge, while the gill holes on the pressure side are inclined at an angle of 45° to the surface where they emerge.

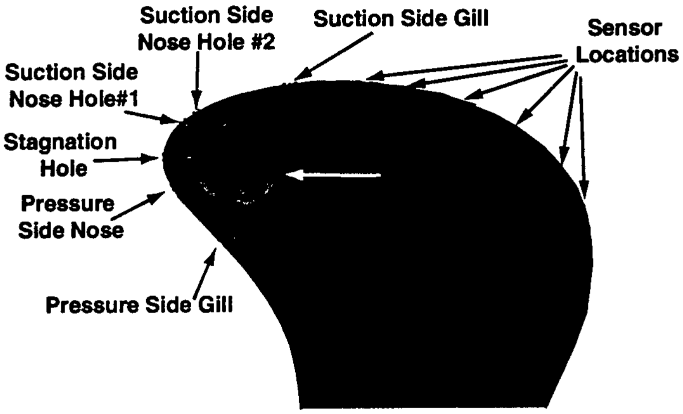

Figure 3: Blade Cooling Scheme

Sensors

Six sets of gauges were press-fit into the blade downstream of the last row of cooling holes on the suction side as can be seen in Fig. 4. Figure 4 is a plan view of the suction side of the blade showing the locations of the cooling hole exits and gauge locations. Each set of gauges is composed of a high-speed pressure transducer (Kulite XCQ-062-50a), a high-speed heat flux and temperature sensor (HFM-7), and a surface-mounted thermocouple. The Kulite transducers are used to acquire high-speed static pressure measurements on the blade surface. The HFM-7's acquire separate, direct and simultaneous measurements of both the local heat flux and wall temperature. The HFM-7 has a gauge diameter of 5mm and an active diameter of 4mm. A detailed discussion of these gauges can be found in Diller (1993). The surface-mounted thermocouple is used as a calibration tool for the HFM-7's temperature sensor. The first set of gauges was mounted approximately 9.1 hole diameters downstream of the last row of cooling holes and the subsequent sets of gauges were staggered along the span and in the streamwise direction. All of the gauges were mounted within a three-inch wide section of the blade span which surface oil flow visualizations had shown to be free of endwall effects. The high thermal conductivity gauge substrates (aluminum nitride) were press fit into the aluminum blade to minimize the fluid and thermal disruptions of the surface. The effect of a possible sensor mismatch with the surface contour was investigated by Peabody and Diller (1998) and deemed to be negligible for this case. Coolant temperature measurements were made with very small exposed junction thermocouples protruding into the exit of the last set of cooling holes. The values were mass-averaged and compared with the coolant temperature in the insulated plenum. The temperatures throughout the coolant supply were tested for uniformity.

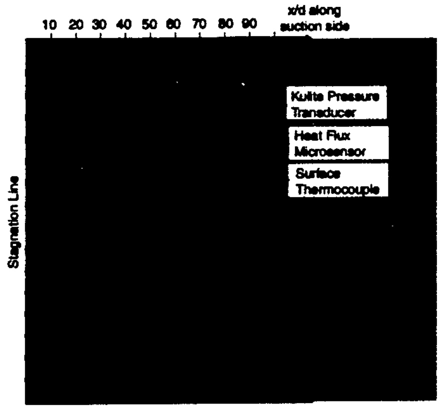

Figure 4: Plan View of the Suction Side Showing Blade Instrumentation and Coolant Exits

Coolant Supply System

A schematic of the coolant system is shown in Fig. 5. Air is supplied to the insulated plenum of the instrumented blade from a large storage tank. The coolant supply storage tank is fed by a 5 hp compressor with a filter and dryer system attached. When air is released from the storage tank it passes through a coolant control system. This coolant control maintains the plenum-to-freestream total pressure ratio over the course of the run via an integral feedback control. Controlling the pressure ratio allows the momentum ratio to be controlled, but the density and blowing ratios vary over a run. The air then flows through an orifice plate, where the mass flow rate is monitored, and into a chiller which uses liquid nitrogen as a coolant. The cold air is then fed into the insulated plenum of the blade.

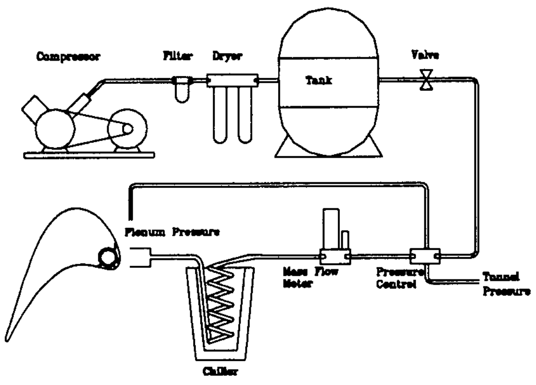

Figure 5: Schematic of Coolant System

DATA ANALYSIS AND RESULTS

Three different types of experiments are presented here. The first type, uncooled runs, used a plenum that was plugged with a plastic insert to block coolant flow during the run and to insure that no mainstream flow bled through different rows of coolant holes. The second type, cooled runs, used the coolant flow at the design pressure ratio of 1.04. Lastly, a third set of experiments were performed where the pressure ratio was varied over the range 1.02 to 1.20 in order to investigate effect of pressure ratio on both the heat transfer coefficient and film cooling effectiveness.

Uncooled Data Analysis and Results

The dominant mode of heat transfer in gas turbines is convection, and the convection heat transfer coefficient is defined by the equation,

$$q = h \cdot (T_{aw} - T_w) \tag{1}$$

where the difference between the adiabatic wall temperature, T_{aw}, and the wall temperature, T_w, is the driving force of the heat transfer. For high-speed flows with no film injection, T_{aw} is equivalent to the recovery temperature, T_r, and equation (1) can be rewritten as,

$$q = h \cdot (T_r - T_w) \tag{2}$$

The recovery temperature can be related to the freestream total temperature by the recovery factor and the freestream velocity,

$$T_t - T_r = (1 - r) \cdot \frac{u^2}{2 \cdot C} = T_d \tag{3}$$

where r is the recovery factor, u is the freestream velocity, and C is the specific heat of air. The difference between the freestream total temperature and the recovery temperature is a constant during the run and will hereafter be referred to as T_d. The recovery factors for laminar and turbulent boundary layers are usually considered to be $Pr^{1/2}$ and $Pr^{1/3}$, respectively [Kays and Crawford, 1993]. Substituting equation (3) into (2) yields,

$$q = h \cdot (T_t - T_w) - h \cdot T_d \tag{4}$$

In equation (4), the local heat flux, q, is the dependent variable and the temperature difference, $T_t - T_w$, is the independent variable. The heat transfer coefficient is the slope in this equation and T_d is equal to the temperature difference, $T_t - T_w$, when $q = 0$ (i.e. the x-axis intercept). It was shown by Popp et al. (1999) that the heat transfer coefficient and T_d did not significantly depend upon the temperatures involved in equation (4). Therefore, for the uncooled case, the heat transfer coefficient and the temperature difference T_d can be obtained by measuring the freestream's total temperature, the blade's wall temperature, and the local heat flux into the blade over the course of an experiment.

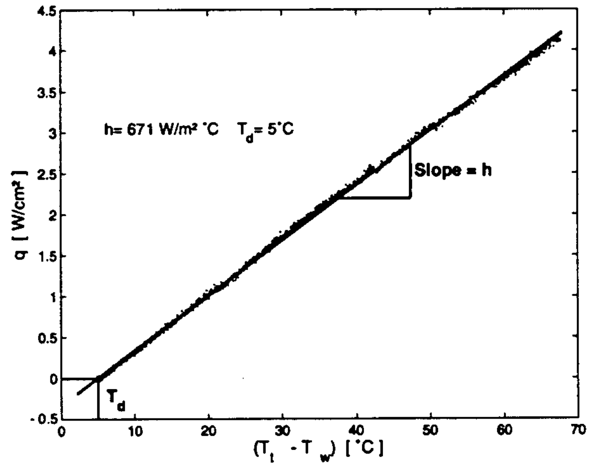

Figure 6: Uncooled Data Analysis (Gauge Location 1)

When the experimental data was fitted to equation (4), the result was a linear trend as can be seen in Fig. 6. Figure 6 is a typical result of the analysis performed on data gathered at the first gauge location. A regression analysis was performed to fit a straight line through this data. The heat transfer coefficient was obtained from the slope of this line, and the temperature difference T_d was determined from the x-axis intercept.

A typical time history of all relevant temperatures, heat flux and the heat transfer coefficient from gauge location 1 can be seen in Fig. 7. The recovery temperature in this figure is determined as a drop from the measured freestream temperature using the calculated local value of T_d (shown in Fig 6). The freestream's total temperature is seen to vary significantly over the course of the experiment. Typically, it varies from 100°C to 30°C as the passive heat exchanger cools down. The blade wall temperature rises approximately 8°C over the course of the run. The time history of the heat transfer coefficient was calculated from the corresponding time histories of T_r, T_w, and q, using equation (2). It can be seen that the heat flux into the blade approaches zero as the recovery and wall temperatures converge, which is consistent with the definition of heat flux in equation (2).

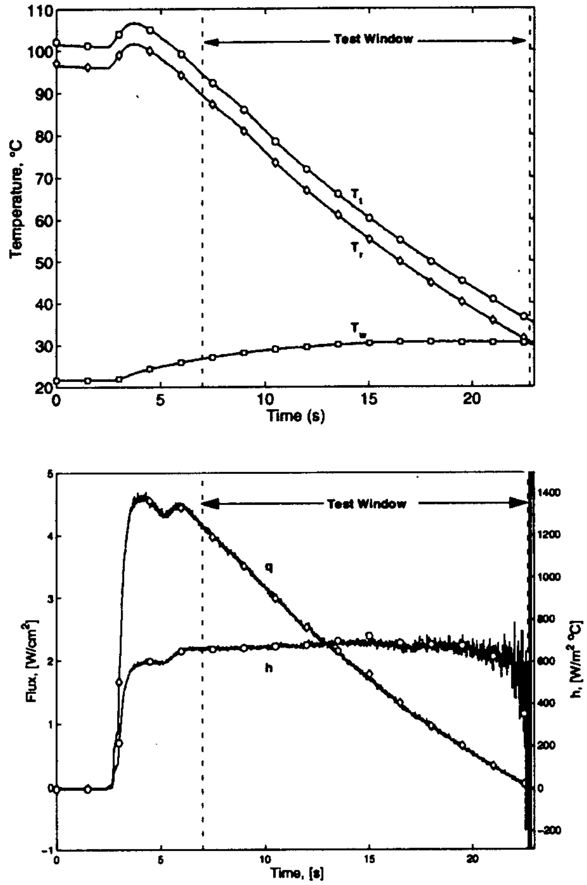

Figure 7: Time History of T_t, T_r, T_w, q, and h
(Uncooled Run, Dashed Lines Indicate Useful Range of Data)

Six experimental runs were performed without film cooling. Figure 8 shows the heat transfer coefficients determined at each gauge location for all six runs. The average level of the heat transfer coefficient over the region of interest was 700 W/m²·°C. The trend of the heat transfer coefficient profile was suspected to be caused by transition of the boundary layer. However, the same trend was still observed during experiments with the suction side boundary layer tripped at the leading edge.

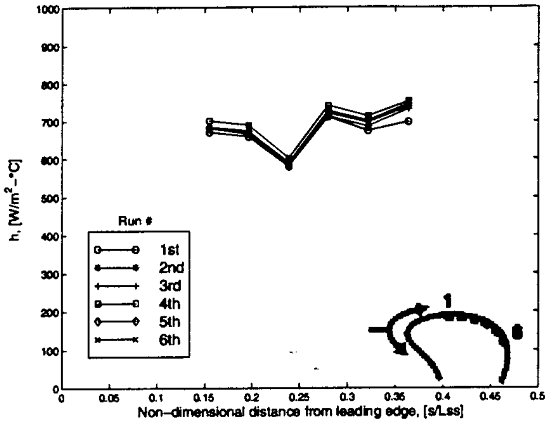

Figure 8: Heat Transfer Coefficient Profile (Uncooled Run)

Film Cooled Data Analysis and Results

For the film cooled experiments, it was important to be able to visualize the condition of the coolant film. The optical access of the cascade test section allowed both shadowgraph and Schlieren photographs to be made in order to visualize the film cooling layer. A high-speed digital camera was used to capture the shadowgraph shown in Fig. 9. The coolant film is clearly attached and turbulence is evident in the film layer on the suction side. The pressure side of the blade is obscured by equipment outside of the test section. Although not evident in this photograph, the stagnation point has shifted slightly towards the suction side, causing the coolant jets exiting the nose holes to be diverted entirely to the pressure side. This did not noticeably alter the pressure distribution around the blade, but none of the coolant from the stagnation holes flowed to the suction side of the blade for cooling. Therefore, only the three rows of coolant holes on the suction side provide protection for the suction side of the blade.

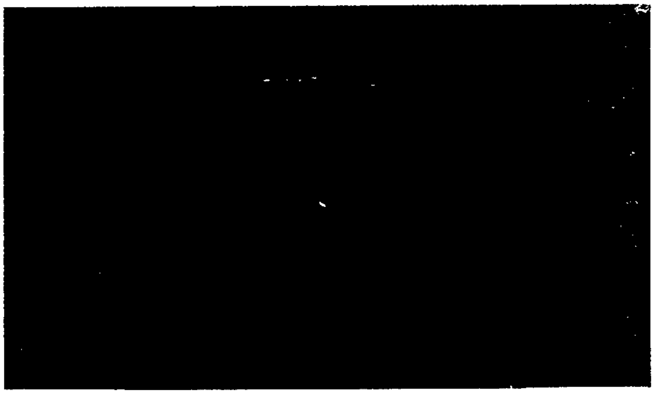

Figure 9: Shadowgraph of Cooling Film

With the addition of film cooling to the surface of a turbine blade in a high-speed flow, the governing equation of convection heat transfer is once again equation (1). However, in such cases the adiabatic wall temperature is usually non-dimensionalized using the adiabatic film effectiveness defined as

$$\eta = \frac{T_{aw} - T_r}{T_c - T_r} \qquad (5)$$

where η is the adiabatic film effectiveness. Equation (5) can be solved for T_{aw} and then substituted into equation (1) which will yield,

$$\frac{q}{T_r - T_c} = h \cdot \left[\frac{T_r - T_w}{T_r - T_c}\right] - h \cdot \eta \qquad (6)$$

The dependent variable in equation (6) is the heat flux divided by a temperature difference and the independent variable is a ratio of two temperature differences. When the experimental results are plotted using these variables, the slope of equation (6) is the heat transfer coefficient and the x-axis intercept gives the adiabatic film effectiveness. Using the values of T_d determined for each gauge position in the uncooled case, the recovery temperatures at each location were calculated from the freestream total temperature.

The experimental data from a typical film cooled run were fitted to equation (6) and the result is a linear trend, which is displayed in Fig. 10. A regression analysis was performed to fit a line through the data. The film cooled heat transfer coefficient was determined from the slope of the line and the adiabatic film effectiveness was obtained from the x-axis intercept. The resulting values do not appear to be a function of temperature. For the same gauge location as shown earlier in the uncooled case, the heat transfer coefficient has increased to 950 W/m^2·°C, while the effectiveness is 31%.

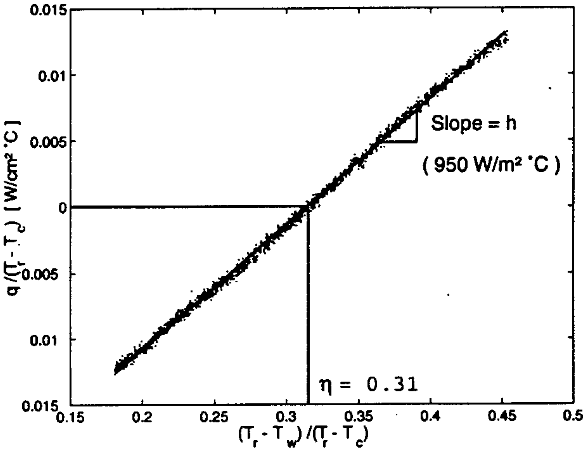

Figure 10: Film cooled Data Analysis

A sample time history of a film cooled run can be seen in Fig. 11. The test window indicates the limits of the data set that were used in the film cooled analysis. The traces in Fig. 11a are similar to those in Fig. 7a except for the addition of a mass-averaged coolant temperature. The adiabatic wall temperature is calculated using the film effectiveness determined from Fig. 10 and equation (5). The freestream temperature again falls from around 100°C to 30°C, while the blade temperature rises from near 0°C to about 10°C. The liquid nitrogen heat exchanger allows the coolant temperature to be maintained at temperatures ranging between −120°C and −150°C. In comparing Figs. 11a and 7a, it should be noted that the driving temperature of the heat transfer is lower for the film cooled case than for the uncooled case. Figure 11b shows that even though the heat transfer coefficient at location 1 increases, the adiabatic wall temperature is lowered enough that the peak level of the heat flux decreases from 4.5 W/cm^2 to 3.5 W/cm^2.

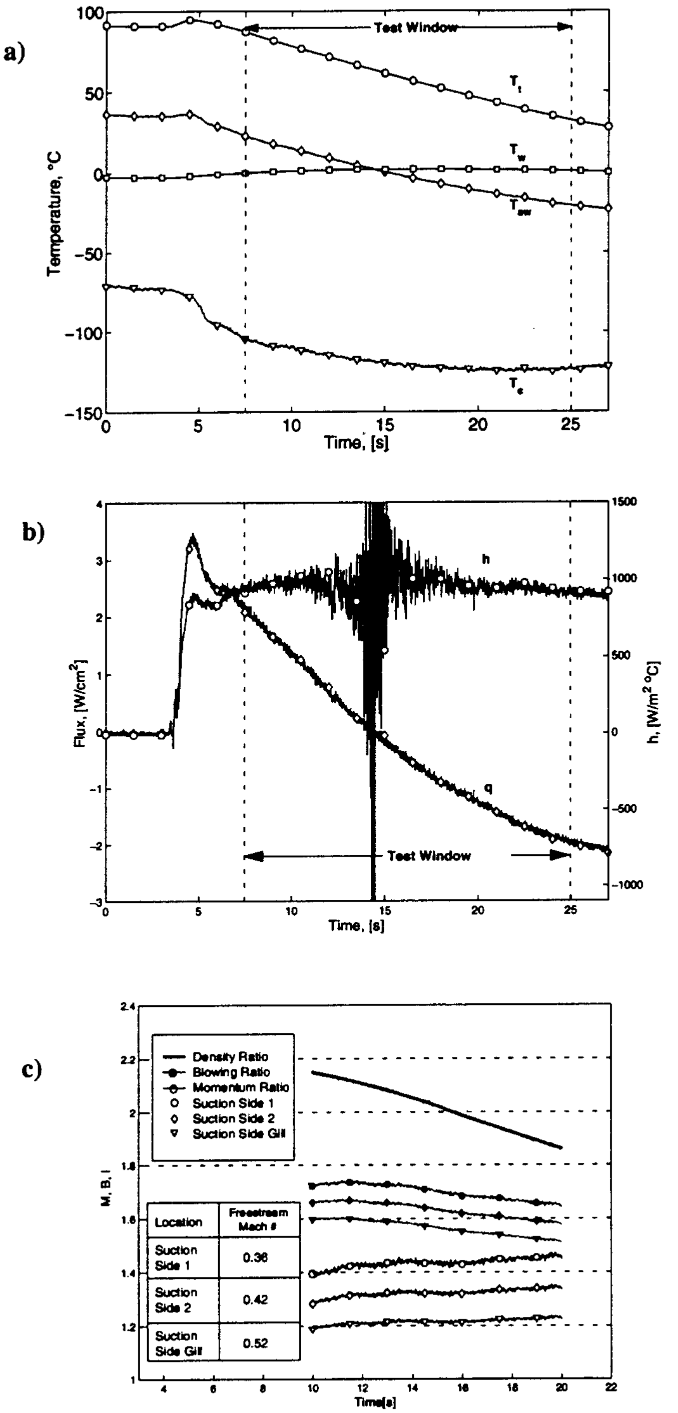

Figure 11: Time Histories for a Film cooled Run (a) All Relevant Temperatures
(b) Heat Flux and Heat Transfer Coefficient
(c) Density Ratio, Blowing Ratio, and Momentum Ratio
(Dashed Lines Indicate Useful Range of Data)

The adiabatic wall temperature was used in equation (1) along with the heat flux and wall temperature to generate the time history of the film cooled heat transfer coefficient seen in Fig. 11b. A singularity occurs in the calculation of the film cooled heat transfer coefficient when T_{aw} and T_w converge. Aside from the singularity, the film cooled heat transfer coefficient is fairly constant over the course of the experiment.

Figure 11(c) shows the coolant-to-freestream density ratio and pressure ratio. In addition, Fig. 11(c) shows the blowing ratio and the momentum ratio for the three coolant holes that affect the suction side of the blade. All of these ratios were determined assuming isentropic flow conditions in the freestream.

Six film cooled experimental runs were performed and analyzed in the manner just described. Figure 12 shows the results of heat transfer coefficient and film effectiveness for all six runs. The average level of the heat transfer coefficient for the film cooled case was found to be 850 W/m^2·°C, a 21% increase over the uncooled experiments. The largest increase was at gauge location 1 followed by 2 and 6. The smallest increase due to film cooling was at gauge location 3. Over the region studied, the film had an average adiabatic effectiveness of 25%. Possible explanations (e.g., transition, gauge calibration, spanwise variations) for the minimum h and maximum η at gauge location 3 were checked, but none appeared to be the cause. These experiments provide a basis for the unsteady work that will be investigated in Part 2 (Popp, 2000).

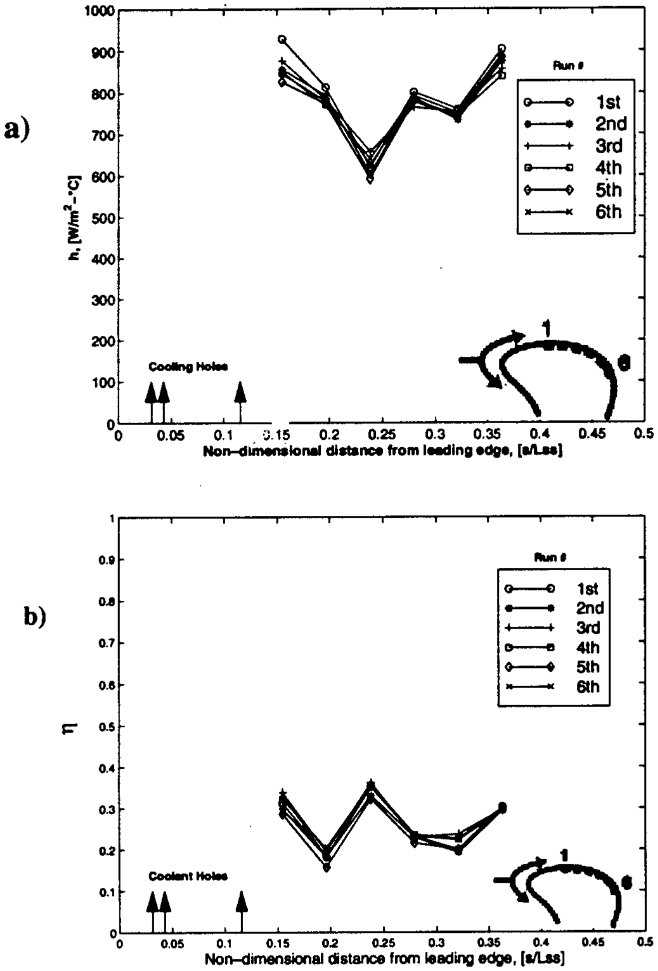

Figure 12: Film Cooled Experiments at a Pressure Ratio of 1.04
(a) Heat Transfer Coefficient, (b) Adiabatic Film Effectiveness

UNCERTAINTY IN h AND η

The theoretical uncertainty for the h and η measurements are divided into two categories; bias and precision uncertainties. The bias uncertainty is composed entirely of the calibration of the heat flux microsensors. The uncertainties and calibration techniques for these gauges are detailed in a paper by Smith et. al. (1999). Separate calibrations were done using convection and radiation and a transient technique was used to check the calibration of each gauge at the start of every test. Table 1 details these bias uncertainties (based on a 90% confidence interval of a student-T distribution).

Gauge	Bias Uncertainty
1	17.0 %
2	3.7 %
3	5.2 %
4	15.2 %
5	8.8 %
6	10.7 %

Table 1: Heat Transfer Coefficient Bias Uncertainties

These gauge bias uncertainties do not effect the bias uncertainty in η since η is determined solely from temperature measurements (i.e. the x-axis intercept in Fig. 10).

Precision uncertainties are comprised of the theoretical variations of temperature measurements and a scheme outlined by Moffat (1988) for calculations involving complex computer algorithms. Based on an individual temperature uncertainty of 1.1°C, this type of analysis yields the precision uncertainties detailed in Table 2.

Gauge	h Precision Uncertainty	η Precision Uncertainty
1	5.9 %	18.5 %
2	6.1 %	21.0 %
3	5.6 %	13.9 %
4	5.9 %	21.3 %
5	6.0 %	17.0 %
6	5.7 %	11.5 %

Table 2: Precision Uncertainties

Another indication of measurement uncertainty is an experimental value of measurement repeatability. This repeatability value was determined from a number of different experiments performed at the same test conditions. The results shown in Table 3 are based on 8 runs at a pressure ratio of 1.04 and a 90% confidence bounds using a student-T distribution.

Gauge	h Repeatability	η Repeatability
1	11.1 %	16.4 %
2	4.0 %	8.2 %
3	5.5 %	7.1 %
4	5.1 %	15.8 %
5	6.7 %	21.1 %
6	7.3 %	11.4 %

Table 3: Measurement Repeatability

THE INFLUENCE OF PRESSURE RATIO ON h AND η

Experiments were performed using the above data reduction technique to determine the influence of the plenum to freestream total pressure ratio on both h and η. Using the coolant control feedback system, the pressure ratio was varied from run to run over the ranges of 1.02 to 1.19. The results from a number of runs are shown in Fig. 13 and Fig. 14. The error bars on these plots indicate the measurement repeatablilty shown in Table 3.

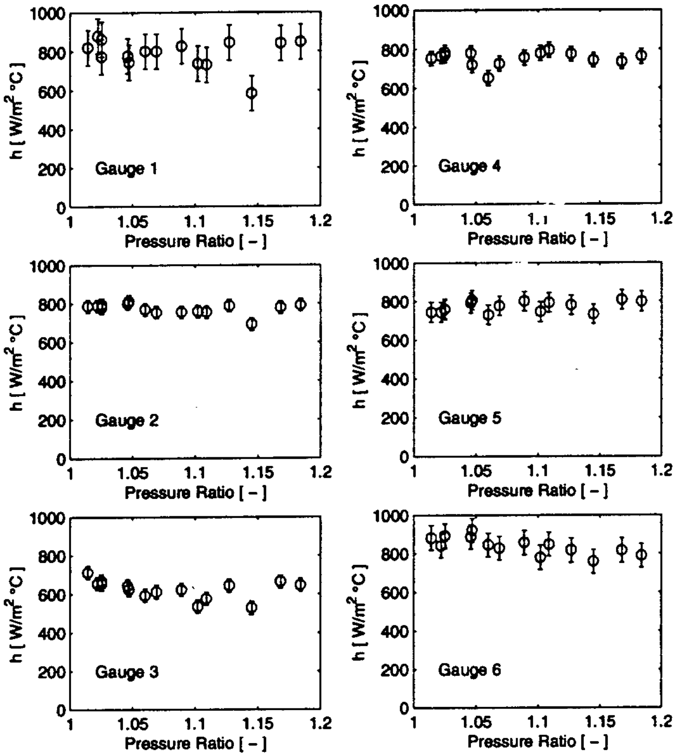

Figure 13: The Influence of Pressure Ratio on the Heat Transfer Coefficient

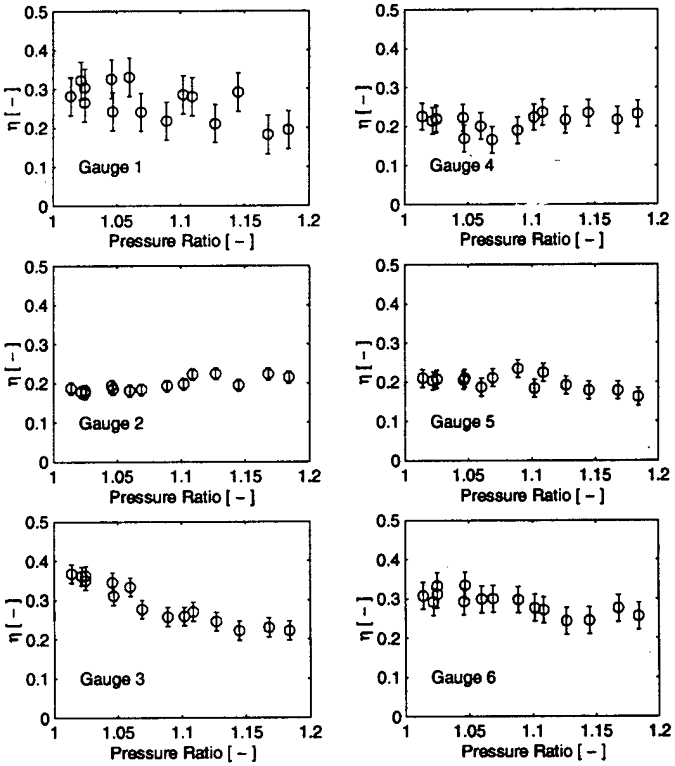

Figure 14: The Influence of Pressure Ratio on Film Cooling Effectiveness

From Fig. 13 it can be seen that, in general, the heat transfer coefficent is fairly independent of the pressure ratio. Also Fig. 14 shows an independence of pressure ratio and effectiveness for gauge locations 2, 4, 5, and 6 and a slight decrease of effectiveness at locations 1 and 3. The slight decrease at these locations is suspected to be attributed to spanwise shifting of the coolant at higher pressure ratios which yielded lower film coverage at these locations.

CONCLUSIONS

Heat transfer experiments were performed on the suction surface of a film cooled transonic turbine rotor blade. A method that allowed for the determination of both the heat transfer coefficient and either the recovery temperature (in uncooled runs) or the film cooling effectiveness (film cooled runs) from one transient run was used. For the nominal pressure ratio of 1.04, an average increase in the heat transfer coefficient of 21% was seen with the addition of film cooling. Varying the pressure ratio in the range from 1.02 to 1.19 had only a weak effect on the heat transfer coefficient and slightly decreased the film effectiveness at some gauge locations.

ACKNOWLEDGMENT

This work was supported by the Air Force Office of Scientific Research (AFOSR) under grant F08671-9601062, monitored by Dr. Jim M. McMichael, Dr. Mark Glauser and Dr. Tom Beutner. We would like to thank Messrs. Scott Hunter, Monty Shelton and Mark Pearson of General Electric Aircraft Engines for their collaboration on this project.

REFERENCES

Abuaf, N., Bunker, R., Lee, C.P., G.E. Aircraft Engines, 1995, "Heat Transfer and Film Cooling Effectiveness in a Linear Cascade," *ASME Journal of Turbomachinery*, Vol. 119, pp. 302-309.

Diller, T. E., 1993, "Advances in Heat Flux Measurement", *Advances in Heat Transfer*, Vol. 23, Eds. J. P. Hartnett et al., Academic Press, Boston, pp. 279-368.

Drost, U., Bölcs, A., Swiss Federal Institute of Technology, 1998, "Investigation of Detailed Film Cooling Effectiveness and Heat Transfer Distributions on a Gas Turbine Airfoil," ASME 98-GT-20.

Ekkad, S.V., Hui Du, and Je-chin Han, 1995, "Local Heat Transfer Coefficient and Film Effectiveness Distributions on a Cylindrical Leading Edge Model Using a Transient Liquid Crystal Image Method," ASME 95-WA/HT-3.

Goldstein, R.J., *Measurements in Heat Transfer*, Hemisphere Pub. Corp., 1976.

Guo, S.M., Lai, C.C., Jeong, J.H., Jones, T.V., and Oldfield, M.L.G., University of Oxford, 1997, "Use of Liquid Crystal Techniques to Measure Film Cooling Heat Transfer and Effectiveness," 90th Symposium of the Propulsion and Energetics Panel, AGARD 20-24.

Guo, S.M., Jones, T.V., University of Oxford, and Lock, G.D., University of Bath, 1996, "Gas Turbine Heat Transfer Measurements with Engine Simulated Film Cooling," 2nd European Conference on Turbomachinery Fluid Dynamics and Thermodynamics, Technological Institute, Section on Aeronautics.

Hale, J. H., Diller, T. E., and Ng, W. F., 1997, "Effects of a Wake on Turbine Blade Heat Transfer in a Transonic Cascade," ASME Paper No. 97-GT-130.

Horton, F.G., Shultz, D.L., Forest, A.E., University of Oxford, 1985, "Heat Transfer Measurements with Film Cooling on a Turbine Balade Profile in Cascade," ASME 95-GT-117.

Kays, W.M. and Crawford, M.E., 1993, *Convective Heat and Mass Transfer*, McGraw-Hill Inc., N. Y., pp 380-388.

Moffat, R. J., 1988, "Describing Uncertainties in Experimental Results", *Experimental and Thermal Fluid Science*, Vol. 1, pp. 3-17.

Peabody, H. L. and Diller, T. E., "Evaluation of an Insert Heat Flux Gage in a Transonic Turbine Cascade," in Proceedings of the ASME Heat Transfer Division – 1998, HTD-Vol. 361-5, ASME, pp. 625-630.

Popp, O., Smith, D., Bubb, J., Grabowski, H., Diller, T., Schetz, J., Ng, W., 1999, "Steady and Unsteady Heat Transfer in a Film cooled Transonic Turbine Cascade," ASME 99-GT-259.

Popp, O., Smith, D., Bubb, J. ., Grabowski, H., Diller, T., Schetz, J., Ng, W., 2000, "Investigation of Heat Transfer in a Film Cooled Transonic Turbine Cascade, Part II: Unsteady Heat Transfer", ASME 2000-GT-203.

Schwarz, S.G., Goldstein, R.J., Eckert, E.R.G., 1990, "The Influence of Curvature on Film Cooling Performance," 35th IGTI Conference, ASME 90-GT-10.

Smith, D., et al., 1999, "A Comparison of Radiation Versus Convective Calibration of Thin-Film Heat Flux Gauges", in Proceedings of the ASME Heat Transfer Division – 1999, HTD-Vol. 364-4, ASME, pp. 79-84.

INVESTIGATION OF HEAT TRANSFER IN A FILM COOLED TRANSONIC TURBINE CASCADE, PART II: UNSTEADY HEAT TRANSFER

O. Popp, D. E. Smith, J. V. Bubb, H. C. Grabowski III, T.E. Diller, J. A. Schetz, W. F. Ng
Virginia Polytechnic Institute and State University
Blacksburg, VA 24061

ABSTRACT

This paper reports on an investigation of the heat transfer on the suction side of a transonic film cooled turbine rotor blade in a linear cascade. A shock wave is generated in a shock tube and passes into the cascade upstream of the blade row to simulate the interaction of a shock emerging from the trailing edge of an upstream nozzle guide vane on the downstream rotating blade row. The unsteady heat transfer caused by the shock wave passing over the suction side of the rotor blade is analyzed and compared to predictive models published in the literature. The investigation includes experiments with and without film cooling and a variation of the most relevant physical parameters. From the analysis and the comparison of the unsteady heat flux it is concluded that the heat transfer coefficient is not affected strongly by the passing shock. Most of the unsteady heat transfer is induced by the variation of temperature caused by the shock wave.

NOMENCLATURE

c_p	specific heat of air
h	heat transfer coefficient w/o film cooling
h_c	heat transfer coefficient w/ film cooling
k	thermal conductivity of air
m	counter in Eq. 9
n	counter in Eq. 9
p	static pressure
q	heat flux per unit area
q_c	unsteady component of heat flux (in Rigby's Model)
q_h	unsteady component of heat flux (in Rigby's Model)
q_M	unsteady component of heat flux (in Moss' Model)
T_{aw}	local adiabatic wall temperature
T_c	coolant exit temperature
T_h	unsteady component of temperature (in Rigby's Model)
T_M	unsteady component of temperature (in Moss' Model)
T_r	local recovery temperature
T_t	freestream total temperature
T_w	local wall or blade temperature
Δt	time between data points
η	film effectiveness defined in Eq.(7)

Superscripts

$'$	unsteady variation

INTRODUCTION

The quest for higher thrust to weight ratios in the development of aero-engines has led to the design of nozzle guide vanes (NGV) with supersonic exit velocities and elaborate film cooling schemes. Consequently, the rotor blades are not only subject to wake but also shock impingement as they pass behind the NGV's at very high rotational speed. The effect of this unsteady process on the heat transfer to the rotor blade has been the topic of a variety of research programs.

Researchers at Texas A&M (Ou et al. (1994), Mehendale et al. (1994), Du et al. (1997)) published time averaged results from a low speed cascade with and without film cooling. Wakes were produced using a spoked wheel rotating upstream of the linear cascade. It was concluded that the presence of the wakes increases the heat transfer coefficient only on the downstream suction side by affecting the transitional behavior of the boundary layer. With the introduction of film cooling on the suction side, the boundary layer is tripped early, and the effect of the wakes decreases accordingly.

Heidmann et al. (1997) presented experimental work on a stationary annular cascade consisting of rotor blades with an inlet Mach Number of 0.27. Wakes were generated using a rotating bar mechanism rotating in front of the cascade. Time-averaged film cooling effectiveness was measured for a showerhead film cooling scheme with two rows of holes at the suction side and the pressure side and one row in the geometric stagnation point. The wake-induced mixing decreased the film cooling effectiveness all along the blade. The effect was more pronounced on the suction side since the swirl generated by the rotating rods shifted the stagnation point. Therefore, more coolant was available on the pressure side, almost outweighing the decrease in film effectiveness due to the increased mixing.

The last in a series of publications on heat flux and pressure measurements in a full stage rotating turbine done at the Calspan-UB Research Center featured phase-locked measurements of heat flux on the rotor blades (Dunn (1989)). No on-rotor pressure measurements were provided to relate the heat flux to the flowfield. On the shroud both pressure and heat flux data were recorded. The fluctuations of heat flux and pressure were shown to be in phase and of similar shape.

In Guenette et al. (1989) a first set of time-resolved on-rotor heat flux and pressure data from a full stage blowdown turbine was reported. The mid section of the rotor blade profile was identical to the blade tested in a linear cascade at the University of Oxford. The data from both setups were compared and showed reasonable agreement. In 1996 Abhari et al. (1996) compared the heat flux results from a steady-state code to time-averaged measurements on a film cooled blade. The presence of the wakes and shocks seemed to decrease the heat transfer on the suction side and increase it on the pressure side.

The most comprehensive body of research was published by the University of Oxford. In 1985 Doorly et al.(1985) were the first to report on time-resolved heat transfer measurements in a linear cascade. A combination of wakes and weak shocks was produced using a rotating bar mechanism. Turbulent spots and bubbles created by shocks and wakes were shown to be responsible for an increase of heat flux. Johnson et al. (1988) used slightly modified blades and increased the rotational speed of the bars to create stronger shock waves. The modified blades were the same ones used by Guenette et al. (1989). The unsteady heat flux caused directly by the impact of the shock wave was observed to be the major contribution to the overall unsteady heat flux. A first version of a predictive model linking isentropic shock heating and one dimensional conduction in the fluid to the unsteady heat flux showed fairly good agreement with measured heat flux data. Rigby et al. (1989) modified this model and gave a thorough derivation. Johnson et al. (1990) found that while the prediction yielded good agreement on the suction side, the pressure side unsteady heat flux was underpredicted. The reason for this was found in a "Vortical Bubble" created by the shock wave and traveling down the pressure side.

Rigby et al. (1990) first included film cooling in the Oxford cascade setup for the investigation of unsteady heat flux. The shock wave signature was found to change with the introduction of film cooling. Data recorded in an entirely new full stage rotating turbine was first published in 1995 by Moss et al. (1995). Time-resolved on-rotor heat flux and pressure measurements were presented. It was shown that the unsteady heat flux could be predicted by multiplying a constant heat transfer coefficient and a temperature variation calculated from the unsteady pressure based on an isentropic assumption. Moss et al. (1997) compared time-averaged heat flux measurements on the rotor with the presence of upstream wakes and a flowfield undisturbed by the nozzle guide vanes. The values of time-averaged heat transfer with and without the presence of upstream disturbances were nearly identical, thus proving the assumption of a constant heat transfer coefficient valid.

Researchers at Virginia Tech have studied in a stationary cascade the individual components of the disturbance from upstream rotating blades. The effects of velocity defect, freestream turbulence, and transient shock impingement were measured in separate experiments to understand the effect of each on turbine blade heat transfer. Hale et al. (1997) modeled the effect of wake passing in a quasi-steady way using a stationary strut that added turbulence and velocity defect. Increases in heat transfer coefficient were measured for a number of locations on the blade, particularly on the pressure side. Nix et al. (1997) analyzed in detail the progression of a shock wave through the same cascade and its effect on the unsteady heat transfer. When averaged over a 200 μs blade passing event, a maximum increase of heat flux of 60% was measured due to shock passing. Popp et al. (1999) presented time-resolved heat flux and pressure data from one measurement location on the suction side of a film cooled transonic rotor cascade. It was shown that the heat transfer coefficient as well as the film cooling effectiveness were not affected significantly by the passing shock wave.

The intent in the present study is to extend the investigation of shock effects to a larger number of measurement locations and to verify the conclusions for a variety of physical parameters for a film cooled blade. The unsteady heat flux will be analyzed to find the relative magnitudes of unsteady heat transfer coefficient, unsteady temperature and film effectiveness and their contributions to the overall unsteady heat flux. Also, the experimental data will be compared to predictive models developed by Rigby et al. (1989) and Moss et al. (1995).

EXPERIMENTAL APPARATUS

Wind Tunnel Facility, Cascade and Shock Apparatus

The experiments necessary for this investigation were performed in the transonic blowdown wind tunnel at Virginia Tech. A passive heating device is available to achieve high (120°C) inlet temperatures to the cascade. It consists of many copper tubes that are preheated prior to running the tunnel. Fig. 1 of Part I (Smith et al. (2000)) shows the wind tunnel with the heating loop. With the present cascade, the facility allows run times of up to 35 seconds with the inlet pressure controlled. The test-section and cascade built for this investigation are shown in Fig. 2 of Part I (Smith et al. (2000)). The cascade consists of four full and two half blades forming five passages. The blade design is a generic, high-turning, first stage rotor geometry. It is scaled up three times to accommodate the cooling scheme and instrumentation. The span is 15.3 cm (6") and the aerodynamic chord is 13.6 cm (5.4"). Pitch and axial chord are 11.4 cm (4.5"). The Reynolds Number based on aerodynamic chord (13.6 cm) and unheated exit conditions is about $6 \cdot 10^6$. The Mach number distribution was shown to correspond to design conditions (Hale et al., 1997).

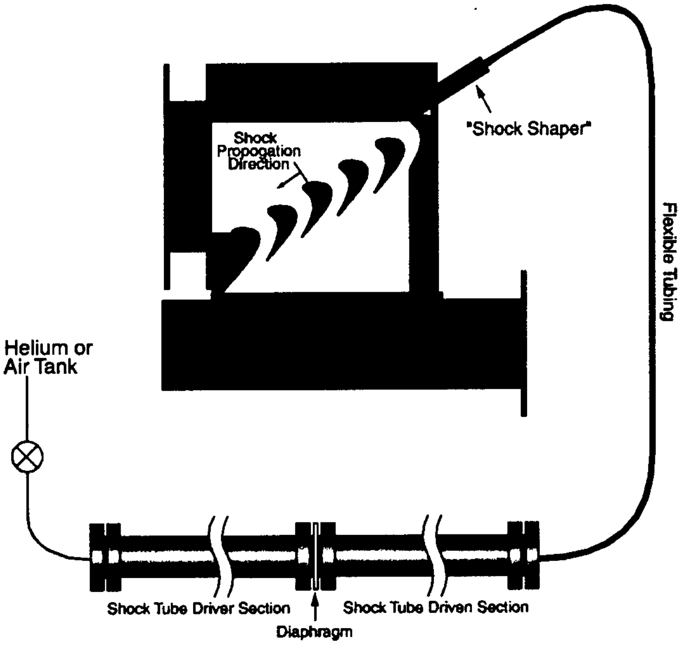
"Shock Shaper"
Shock Propogation Direction
Flexible Tubing
Helium or Air Tank
Shock Tube Driver Section
Shock Tube Driven Section
Diaphragm

Figure 1: Cascade and Shock Apparatus

To simulate the shock emerging from the trailing edge of a NGV, a shock tube creates a shock wave which is sent through flexible tubing and along the leading edges of the cascade (see Fig. 1). The shock strength can be varied to obtain realistic pressure ratios by mounting diaphragms of different thickness between the driver and driven section of the shock tube.

Cooling Design

A schematic of the showerhead film cooling design is shown in Fig. 3 in Part I (Popp et al., 2000). The design is a generic showerhead layout with four rows of holes close to the leading edge and a row of "gill" holes on both pressure and suction side. The rows around the leading edge are normal to the chordwise tangent and inclined 30° with respect to the spanwise direction. The "gill" row on the suction side is normal to the spanwise direction and inclined 30° with respect to the chordwise tangent while the "gill" row on the pressure side emerges at an angle of 45°. All holes are fed by a common plenum which is insulated to reduce internal heat transfer. The coolant supply and coolant pressure control is shown in Fig. 5 in Part I. This setup allows the control of the ratio of coolant total pressure to freestream total pressure. This corresponds to the Momentum Ratio, since air is used as the coolant. The objective temperature ratio T_t/T_c was 2, but was allowed to vary during the run. Therefore, the Density Ratio and Blowing Ratio also vary throughout the experiment, while the Momentum Ratio is nearly constant.

Sensors

The six measurement locations are shown in Fig. 3 and 4 in Part I (Popp et al., 2000). At each measurement location a triplet of gauges is installed. A *Kulite* Pressure Sensor XCQ-062-50a is monitoring static surface pressure. A *Vatell* HFM-7/L Heat Flux Microsensor gives a direct reading of surface heat flux and of surface temperature. A surface thermocouple is used as a calibration tool for the resistance temperature device of the HFM-7/L. For the high speed measurements of surface pressure and heat flux, the dynamic characteristics of the heat flux and pressure sensors had to be known. In a shock tube experiment, the transfer function of the *Kulite* XCQ-062-50a pressure sensor with B-screen was found to be modeled well as a second order system in the frequency range of up to 100 kHz. The transfer function of the heat flux sensors was experimentally determined to be of first order with a time constant of about 17μs.

Data Acquisition and Signal Processing

Both surface static pressure and heat flux were recorded at 500 kHz with a *LeCroy* High Speed Waveform Recorder. The signals were filtered at 102.4 kHz using *Frequency Devices* Model 9064 8-Pole Butterworth Low-Pass Filters. Since the transfer functions of both pressure and heat flux sensors show significant signal attenuation and phase shift in the frequency range below the cut-off frequency, the recorded signals were corrected. The transfer functions that had been determined experimentally were inversely applied to the pressure and heat flux data (Popp, 1999).

To find the mean heat flux before shock impact, a time window of 5 μs before the sudden rise in heat flux was used for averaging.

Test Matrix

A technique for the analysis of the transient heat transfer due to shock passing was presented in Popp et al. (1999). This technique will be applied to heat flux time histories in the section "Unsteady Decomposition". The analysis was done with and without film cooling and under a wide variety of parameters. Without film cooling, two parameters were varied: Shock strength and heat flux before shock impact. The shock strength was varied in two steps. In terms of peak static pressure ratio at gauge #2 the recorded peak values of shock strength were 1.2 and 1.3 when the pressure signal was filtered at 25 kHz.. The level of heat flux before shock impact was varied by triggering the shock at different times during the tunnel run. As seen in Fig. 7 (a) and 11 (a) in Part I, the heat flux level changes during the test. It was attempted to obtain three different levels of initial heat flux (high, medium, low). The two values of shock strength and the three values of heat flux yield a test matrix of six experiments without film cooling. For the tests with film cooling one additional parameter was varied. The ratio of coolant total pressure to freestream total pressure was set to the nominal value (1.04) and a high value (1.2). With the shock strength and the initial level of heat flux varied as in the case without film cooling, this resulted in a test matrix of twelve experiments with film cooling. In section "Unsteady Decomposition" only sample experiments are shown. The conclusions drawn there have been verified for all conditions tested in these test matrices.

In sections "Comparison with Rigby's Model" and "Comparison with Moss' Model", two models predicting unsteady heat flux from surface static pressure are compared to measured heat flux. For this purpose pressure and heat flux time histories had to be sampled and filtered at the same frequencies, and the signals had to be corrected in order to have the same signal attenuation and phase. This was done according to the procedure described briefly in section "Data Acquisition and Signal Processing". For the comparison a separate and shorter series of experiments was done. Pressure and heat flux were only recorded at measurement locations #1 and #2. Two tests with film cooling and one test without film cooling were done at the higher shock strength. Since the frequency content of the pressure data is much wider in these tests (102.4 kHz compared to 25 kHz), the peak unsteady pressure ratio measured at gauge #2 is about 1.5 (compared to 1.3 in the tests with the lower cut-off frequency), while the "real" shock strength is identical. For the two experiments with film cooling, the ratio of coolant total pressure to freestream total pressure was set to the nominal value of 1.04. One test with and one without film cooling are presented.

RESULTS AND DISCUSSION

General Observations

A series of Shadowgraphs taken with a high-speed camera showed no particularly strong interaction between the shock wave and

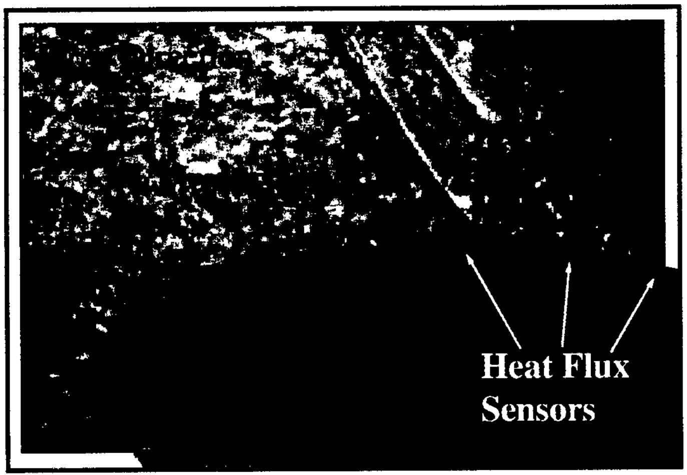

Figure 2: Sample Shadowgraph Illustrating the Interaction between Passing Shock and Layer of Coolant Air

the layer of cooling air. No film detachment or separation was observed. Also no "Separation Bubble" nor "Vortical Bubble" was seen. Fig. 2 shows a sample Shadowgraph of the shock passing process with the shock just above gauge #1.

Samples of the heat flux traces without film cooling are shown for gauges #1 through #5 in the upper graph of Fig. 3. The lower graph in the same figure shows the pressure traces from gauges #2, #4, #5 and #6 from the same experiment. Because most of the pressure traces were only used for visual comparison, the pressure signals shown here were filtered at only 25 kHz. The x-axes on the two graphs are identical to illustrate the time history of the passing shock as it passes over the gauges. The y-axes on each graph are also identical to allow for a comparison of the relative strength of the shock on each gauge. The time mean value of heat transfer before shock impact was removed to show only the unsteady component of the heat flux for better comparison. This figure illustrates that the time histories of pressure and heat flux are in phase and similar in shape. Higher values of unsteady pressure correspond to higher values of unsteady heat flux.

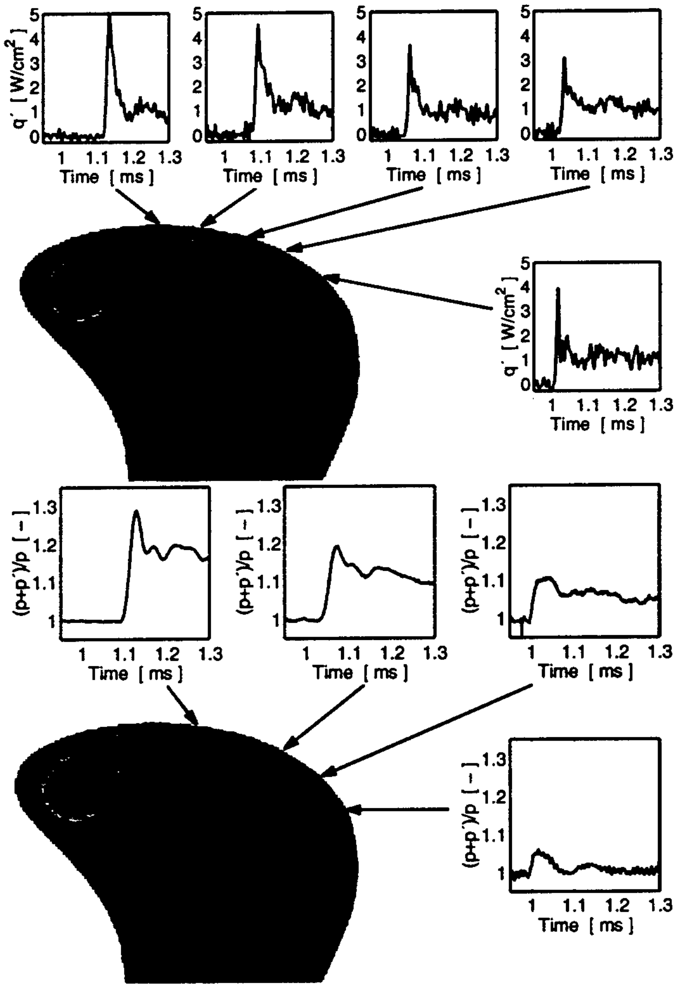

Figure 3: Traces of Unsteady Heat Flux (Upper Graph) and Unsteady Pressure (Lower Graph) Due to Shock Passing Without Film Cooling

The same observation can be made for the experiments with film cooling. The unsteady pressure and heat flux histories from one experiment with film cooling are shown in Fig. 4. When comparing Fig. 3 and 4 it can also be seen that the traces of unsteady pressure and heat flux with and without film cooling appear similar in shape and phase. This is in contradiction to the statement by Rigby et al. (1990), who concluded that "the unsteady shock wave signature changes when film cooling is introduced". For the front suction surface they observed similar but reduced traces of unsteady Nusselt Number with the introduction of film cooling. This observation is supported by Fig. 3 and 4. Even though the pressure traces with and without film cooling are nearly identical the heat flux signatures with film cooling are about 20 to 30% lower.

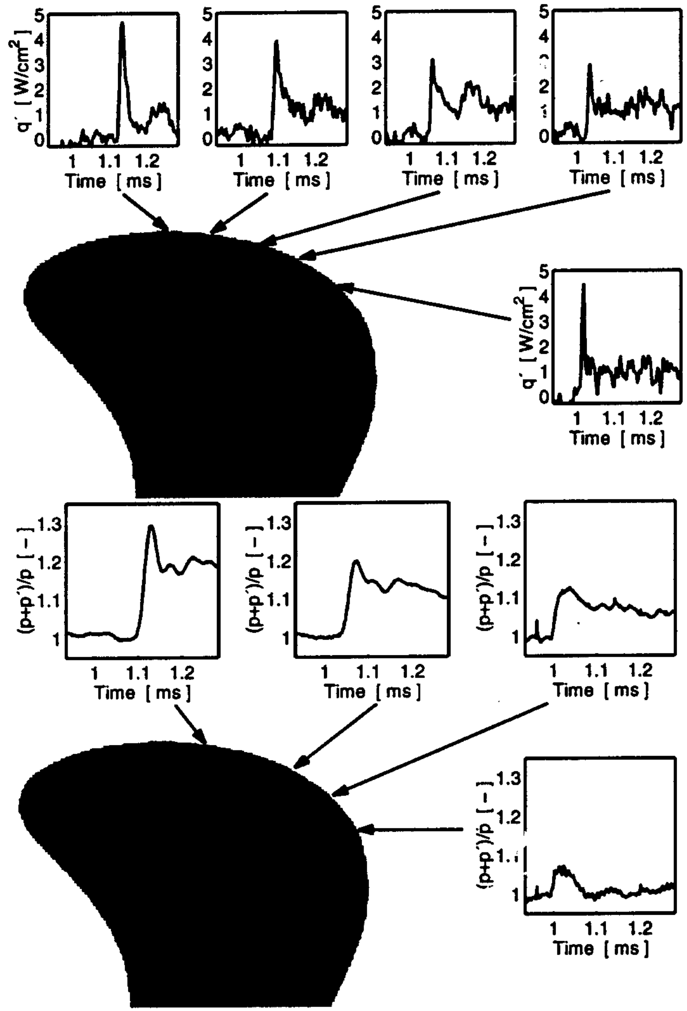

Figure 4: Traces of Unsteady Heat Flux (Upper Graph) and Unsteady Pressure (Lower Graph) Due to Shock Passing With Film Cooling

"Unsteady Decomposition"

The unsteady component of heat flux due to shock passing can be analyzed by a general decomposition of all parameters involved (Popp et al. (1999)). The expression for the unsteady heat flux as a function of all time dependent parameters is then:

$$q' = h' \cdot \left(T_{aw} - T_w\right) + h \cdot T'_{aw} + h' \cdot T'_{aw} \qquad (1)$$

The superscript ′ refers to the unsteady component of the physical parameter while the variables without the superscript refer to the value of the variable before shock impact. In the case without film cooling the adiabatic wall temperature T_{aw} and its time varying component T'_{aw} can be replaced by the recovery temperature and its corresponding time varying function.

Unsteady Variation of Heat Transfer Coefficient. The first term on the right hand side of Eq. 1 shows that the contribution of the unsteady heat transfer coefficient, h´, to the overall unsteady heat flux depends on the temperature difference T_{aw}-T_w before shock impact, or equivalently the heat transfer before shock impact. However, it will be shown in this section that the overall unsteady heat flux is independent of the value of heat flux before shock impact. This implies that the unsteady component of heat transfer coefficient is not contributing significantly to the overall unsteady heat flux. If h´ was of the same order of magnitude as the value of heat transfer coefficient before shock impact, it would have to contribute to the unsteady heat flux by an amount of the order of the value of heat flux before shock impact. This is clearly not the case as seen in Fig. 5 and 6.

Fig. 5 shows the superposition of heat flux data from three different shock passing experiments without film cooling at different levels of initial heat flux (all at the higher shock strength). For each of the five gauges the upper graph shows the sum of the steady and unsteady heat flux due to shock passing. The different levels of q before shock impact can be found in these graphs. In the lower graphs the values of heat flux before shock impingement were removed, yielding the unsteady component of heat flux q´. Fig. 6 shows the same arrangement for three experiments with film cooling (higher shock strength, coolant to freestream total pressure ratio=1.2). It can be seen that the three traces of unsteady heat flux collapse in both cases. **This illustrates that the unsteady component of heat flux is independent of the initial level of heat flux before shock impingement, thereby proving that the contribution of the unsteady heat transfer coefficient to the overall unsteady heat flux is small both with and without film cooling (i.e. h´ is much smaller than h).**

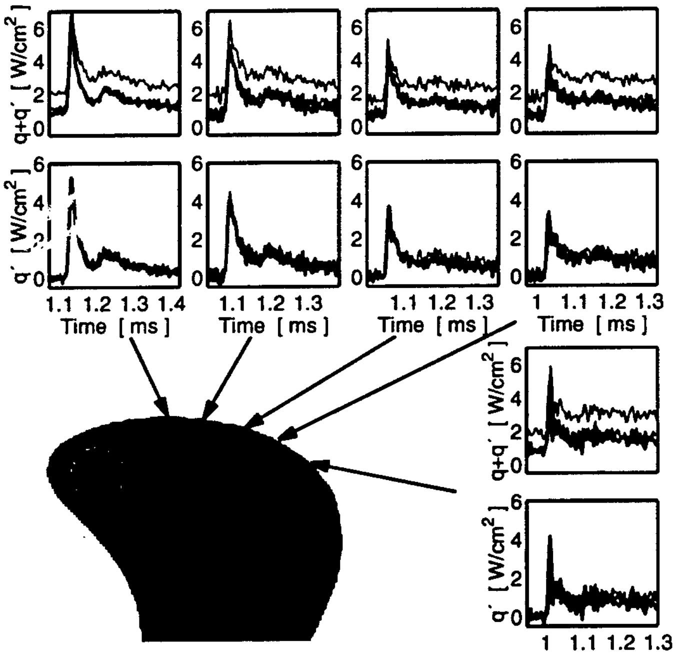

Figure 5: Overall and Unsteady Heat Flux Due to Shock Passing.
Upper Graphs: Overall Unsteady Heat Flux During Shock Impact.
Lower Graphs: Unsteady Component of Heat Flux.
Three Experiments without Film Cooling.
(Shock Pressure Ratio 1.3)

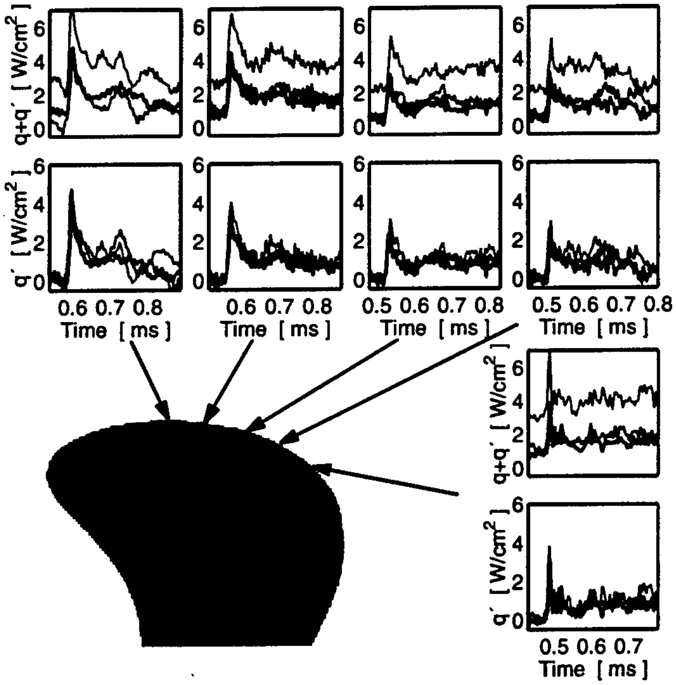

Figure 6: Heat Flux and Unsteady Heat Flux Due to Shock Passing.
Upper Graphs: Overall Unsteady Heat Flux During Shock Impact.
Lower Graphs: Unsteady Component of Heat Flux.
Three Experiments with Film Cooling.
(Shock Pressure Ratio 1.3, Coolant to Freestream Pressure Ratio 1.2)

The terms containing h´ in Eq. 1 can be dropped based on this conclusion. For the experiments without film cooling this yields the following relation between the unsteady variation of recovery temperature and unsteady heat flux:

$$q' = h \cdot T_r' \quad \text{or} \quad T_r' = \frac{q'}{h} \tag{2}$$

For the experiments with film cooling the corresponding relation is:

$$q' = h_c \cdot T_{aw}' \quad \text{or} \quad T_{aw}' = \frac{q'}{h_c} \tag{3}$$

These equations imply that all the unsteady heat flux is caused by a temperature variation induced by the passing shock, which follows from the conclusions drawn above.

Unsteady Variation of Film Effectiveness. The effect of the passing shock on the film effectiveness can be analyzed by decomposing the unsteady variation of adiabatic wall temperature according to Popp et al.(1999):

$$T_{aw}' = T_r' \cdot (1-\eta) - \eta' \cdot (T_r - T_c) - \eta' \cdot T_r' \tag{4}$$

Or rearranged:

$$\eta' \cdot [(T_r - T_c) + T_r'] = T_r' \cdot (1-\eta) - T_{aw}' \tag{5}$$

The difference between the variation of the recovery temperature scaled by (1-η) and the variation of adiabatic wall temperature is a measure for the magnitude of η′. The scaling factor for η′ on the left hand side of Eq. 5 is always a relatively high number since the difference between the recovery and the coolant temperature is of the order of 150°C. To estimate the magnitude of η′, the two terms on the right hand side of Eq. 5 are plotted in Fig. 7. T'_r is calculated from an uncooled experiment shown in Fig. 5 using Eq.2. The results for T'_r are so similar for the three experiments that a separate comparison is not necessary and a representative trace of T'_r can be used. The value of η used for each gauge location is the local mean value of η from all three experiments. The actual values were determined according to the procedure explained in Part I of this paper (Popp et al., 2000).

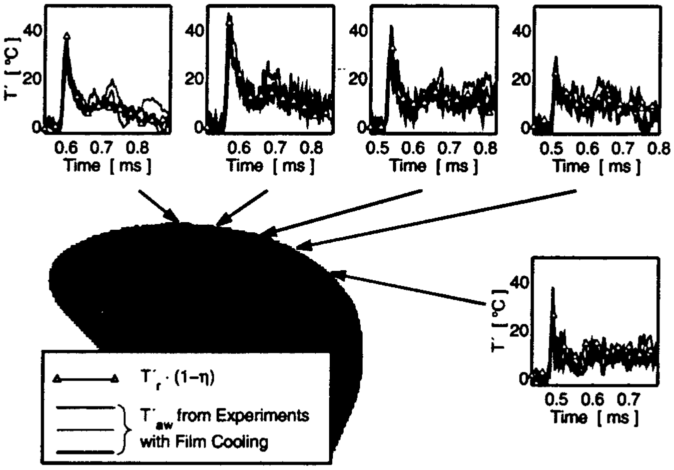

Figure 7: Comparison of $T'_r(1-\eta)$ and T'_{aw} for Three Different Film Cooled Experiments.

It can be seen from Fig. 7 that the difference between $T'_r(1-\eta)$ and T'_{aw} does not exceed 7°C at all times in all three experiments and the five gauge locations. With $[(T_r-T_c)+T'_r]$ on the order of 150°C this will yield values of η′ not exceeding 5%. This value is relatively small compared to the value of η (on the order of 20% to 30%). The variation of the film effectiveness can therefore be considered a secondary effect in the heat transfer process of shock passage.

Comparison with Rigby's Model

In 1989 Rigby et al. (1989) published a modified version of a model for the prediction of unsteady heat transfer first developed by Johnson et al. (1988). The two models are very similar but the later version came with a more thorough derivation. Therefore, Rigby's model will be used for comparison with the data presented here. The reader is referred to Rigby et al. (1989) for the detailed derivation. Two components of unsteady heat flux are identified. One of them is caused by compression of the boundary layer:

$$q_c = q\cdot\left(\frac{p+p'}{p}\right) \tag{6}$$

The second component of unsteady heat flux is caused by transient conduction in the fluid close to the wall. Neglecting convective and viscous terms in the boundary layer equation it is found that the one-dimensional heat conduction equation applies to this component of surface heat flux. The temperature time history used to find this component of heat flux is expressed as:

$$T(0,t) = T_w\cdot\left[\left(\frac{p+p'}{p}\right)^{\frac{\gamma-1}{\gamma}}-1\right] \tag{7}$$

This temperature time history is processed according to Oldfield et al (1978) to yield the second component of unsteady heat flux q_h:

$$q_h(t_m)=\frac{2\cdot\sqrt{k\cdot\rho\cdot c_p}_{gas}}{\sqrt{\pi\cdot\Delta t}}\cdot\sum_{n=2}^{m-1}\left(T_{n+1}-2\cdot T_n+T_{n-1}\right)\cdot\sqrt{m-n} \tag{8}$$

The overall heat flux can be calculated using:

$$q+q' = q_c + q_h \tag{9}$$

The method is illustrated in Fig. 8 for an experiment without film cooling. Only data from gauges #1 and #2 are available for this type of comparison. The graphs on the left hand side of Fig. 8 show data from gauge #1, while the right column of graphs show data from gauge #2. The top graphs show the pressure time history and the time history T(0,t) calculated according to Eq. 7. The second row of graphs show the time history of q_h and q_c determined according to Eqs. 8 and 6 respectively. The last row of graphs shows the direct comparison of the measured and predicted heat flux. The time histories of measured heat flux and surface pressure were both compensated for their specific transfer functions in the frequency range below 102.4 kHz.

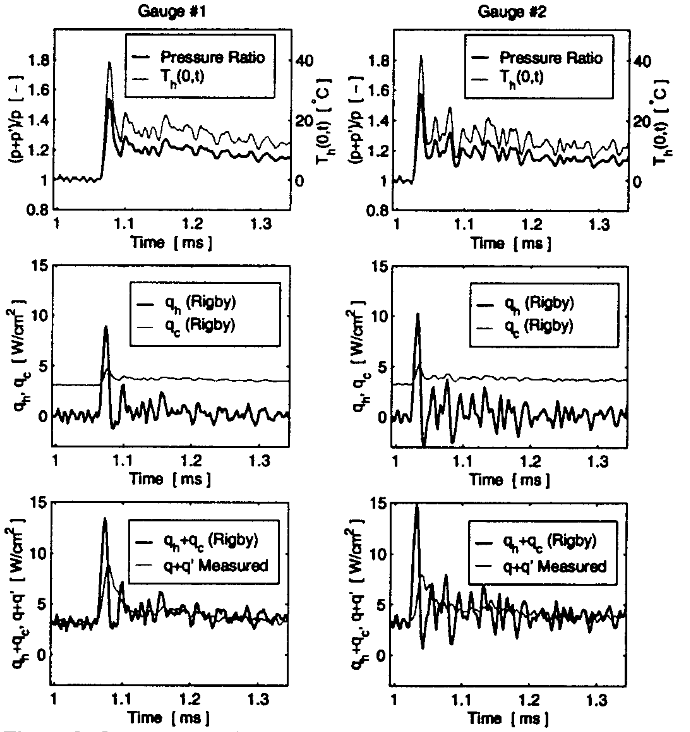

Figure 8: Comparison of Measured Heat Flux and Heat Flux Predicted According to Rigby's Model (Experiment without Film Cooling).
Left Column: Gauge #1.
Right Column: Gauge #2.
Top Row: Time Histories of Pressure and $T_h(0,t)$.
Middle Row: q_h and q_c.
Bottom Row: Comparison of Measured and Predicted Heat Flux.

From the second row of graphs it is clear that the shock effect on q_h is much larger than on q_c for the levels of q and the pressure ratios encountered in these experiments. The last row of graphs showing the direct comparison between the measured and predicted heat flux illustrates that the model overpredicts the unsteady heat flux due to shock passing. The reason for this must be that at least one of the three major simplifications made in the derivation of the model was not justified (neglecting convective and viscous terms, dropping the term containing the time derivative of pressure in Eq. (14) of Rigby et al. (1989)). Fig. 9 shows the same comparison presented in Fig. 8 for an experiment with film cooling. The time histories of pressure are nearly identical with and without film cooling. Therefore, the traces of $T_h(0.t)$ and q_h are also similar, and q_h overpredicts the measured heat flux.

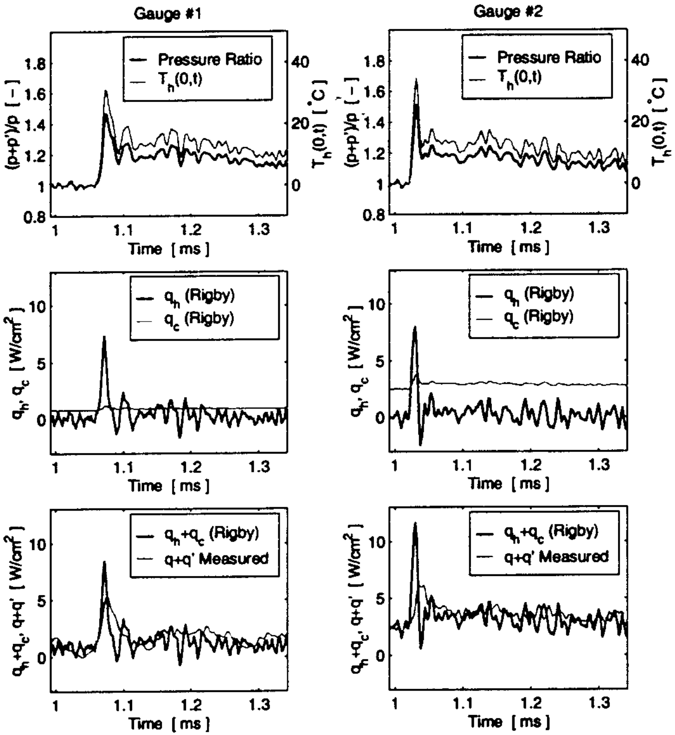

Figure 9: Comparison of Measured Heat Flux and Heat Flux Predicted According to Rigby's Model (Experiment with Film Cooling).
Left Column: Gauge #1
Right Column: Gauge #2
Top Row: Time Histories of Pressure and $T_h(0,t)$
Middle Row: q_h and q_c
Bottom Row: Comparison of Measured and Predicted Heat Flux

Comparison with Moss' Model

In 1995 Moss et al. (1995) published ensemble-averaged heat flux and pressure data from a rotating turbine facility. Using Johnson's model – which is almost identical to Rigby's model – they predicted heat flux from the pressure time histories and found reasonable agreement. By simply assuming a constant heat transfer coefficient and predicting the heat transfer from a temperature variation induced by isentropic compression, an even better prediction could be found:

$$q_M = h \cdot T_M \quad \text{with} \quad T_M = T \cdot \left[\left(\frac{p+p'}{p} \right)^{\frac{\gamma-1}{\gamma}} - 1 \right] \qquad (10)$$

The constant temperature T in Eq. 10 was not specified by Moss et al. (1995). For the comparison in this investigation, the freestream static temperature will be used. Fig. 10 and 11 demonstrate the method and compare the predicted heat flux to the data shown in the last section for an experiment without and with film cooling respectively.

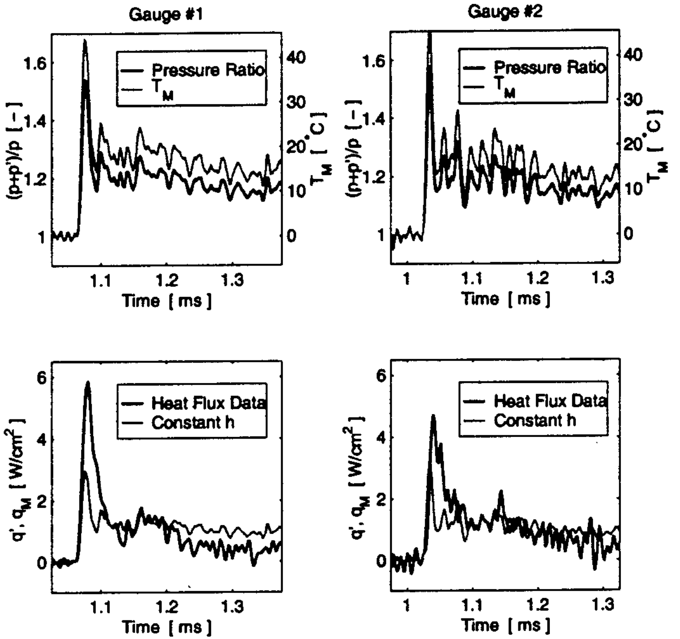

Figure 10: Comparison of Heat Flux Data with Moss' Assumption of a Constant h (Experiment Without Film Cooling).
Left Column: Gauge #1.
Right Column: Gauge #2.
Top Row: Pressure and Temperature Time Histories
Bottom Row: Comparison of Measured and Predicted Heat Flux

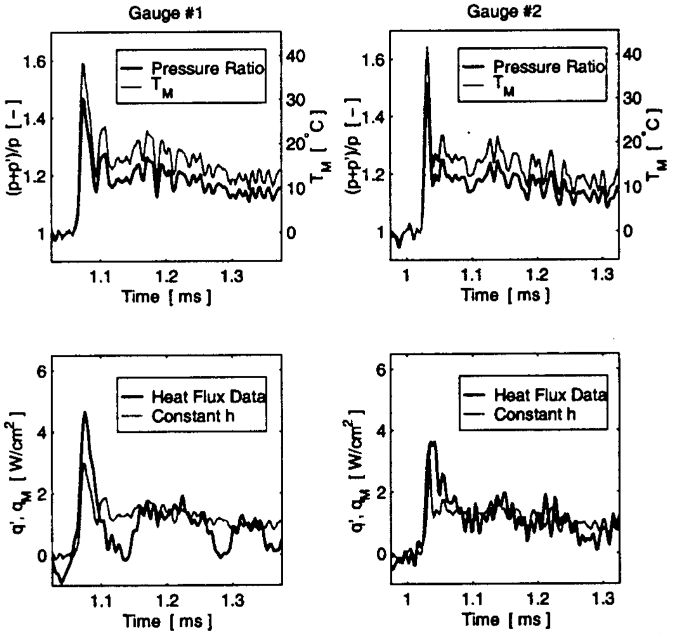

Figure 11: Comparison of Heat Flux Data with Moss' Assumption of a Constant Heat Transfer Coefficient (Experiment With Film Cooling).
Left Column: Gauge #1
Right Column: Gauge #2
Top Row: Pressure and Temperature Time Histories
Bottom Row: Comparison of Predicted and Measured Heat Flux

Moss' prediction matches the measured heat flux much better in terms of magnitude and shape than Rigby's model presented in the last section, even though it slightly underpredicts the initial peak. The conclusion from section "Unsteady Decomposition" is supported by this observation. The contribution of the variation of the heat transfer coefficient to the overall unsteady heat flux proves to be small compared to the unsteady heat transfer caused by the variation of temperature induced by the passing shock.

CONCLUSIONS

The unsteady heat transfer caused by a passing shock wave on the suction side of a transonic turbine blade was investigated with and without film cooling. Heat flux data was analyzed by means of a mathematical decomposition and by comparison with predictive models available in the literature. The mathematical and comparative analysis leads to the conclusion that the unsteady heat transfer is mostly driven by the temperature fluctuation induced by the passing shock wave. Heat transfer coefficient and film effectiveness are not affected enough to contribute significantly to the overall unsteady heat transfer. This conclusion was verified on six locations on the suction side for shocks of different strength and for different coolant blowing rates. Since the temperature in an actual engine is fluctuating around its mean value, the time mean heat transfer in the presence of shocks is expected not to differ significantly from the time mean heat flux without the disturbance of the shock.

ACKNOWLEDGMENT

This work was supported by the Air Force Office of Scientific Research (AFOSR) under grant F08671-9601062, monitored by Dr. Jim M. McMichael, Dr. Mark Glauser and Dr. Tom Beutner. We would like to thank Messrs. Scott Hunter, Monty Shelton and Mark Pearson of General Electric Aircraft Engines for their collaboration on this project.

REFERENCES

Abhari, R.S, 1996,"Impact of Rotor-Stator Interaction on Turbine Blade Film Cooling", *ASME Journal of Turbomachinery*, Vol. 118, pp. 123-133

Doorly, D.J., Oldfield, M.L.G., 1985,"Simulation of the Effects of Shock Passing on a Turbine Rotor Blade", ASME 85-GT-112

Du, H., Han, J.-C., Ekkad, S.V., 1997, "Effect of Unsteady Wake on Detailed Heat Transfer Coefficient and Film Effectiveness Distributions for a Gas Turbine Blade", ASME 97-GT-166

Dunn, M.G., 1989, "Phase and Time-Resolved Measurements of Unsteady Heat Transfer and Pressure in a Full-Stage Rotating Turbine", ASME 89-GT-135

Guenette, G.R., Epstein, A.H., Giles, M.B., Haimes, R., 1989, "Fully Scaled Transonic Turbine Rotor Heat Transfer Measurements", *ASME Journal of Turbomachinery*, Vol. 111, pp. 1-7

Hale, J.H., Diller, T.E., Ng, W.F., 1997, "Effects of Wake on Turbine Blade Heat Transfer in a Transonic Cascade", ASME 97-GT-130

Heidmann, J. D., Lucci, B.L., Reshotko, E., 1997, "An Experimental Study of the Effect of Wake Passing on Turbine Blade Film Cooling", ASME 97-GT-255

Johnson, A.B., Rigby, M.J., Oldfield, M.L.G., Ainsworth, R.W., Oliver M.J., 1988, "Surface Heat Transfer Fluctuations on a Turbine Rotor Blade Due to Upstream Shock Wave Passing", ASME 88-GT-172

Johnson, A.B., Oldfield, M.L.G., Rigby, M.J., Giles, M.B., 1990, "Nozzle Guide Vane Shock Wave Propagation and Bifurcation in a Transonic Turbine Rotor", ASME 90-GT-310

Mehendale, A.B., Han, J.-C., Ou, S., Lee, C.P., 1994, "Unsteady Wake Over a Linear Turbine Blade Cascade With Air and CO2 Film Injection: Part II – Effect on Film Effectiveness and Heat Transfer Distributions", *ASME Journal of Turbomachinery*, Vol. 116, pp 730- 737

Moss, R.W., Sheldrake, C.D., Ainsworth, R.W., Smith, A.D., Dancer, S.N., 1995, "Unsteady Pressure and Heat Transfer Measurements on a Rotating Blade Surface in Transient Flow Facility", AGARD CP-571, pp. 22-1 – 22-9

Moss, R.W., Ainsworth, R.W., Garside T., 1997, "Effects of Rotation on Blade Surface Heat Transfer: An Experimental Investigation.", ASME 97-GT-188

Nix, A.C., Reid, T., Peabody, H., Ng, W.F., Diller, T.E., Schetz, J.A., 1997, "Effects of Shock Wave Passing on Turbine Blade Heat Transfer in a Transonic Cascade", AIAA-97-0160

Oldfield, M.L.G., Jones, T.V., Schultz, D.L., 1978, "On-Line Computer for Transient Turbine Cascade Instrumentation, *IEEE Transactions on Aerospace and Electronic Systems*, Vol. AES-14, No. 5, pp. 738-749

Ou, S., Han, J.-C., Mehendale, A.B., Lee, C.P., 1994,"Unsteady Wake Over a Linear Turbine Blade Cascade With Air and CO2 Film Injection: Part I – Effect on Heat Transfer Coefficients", *ASME Journal of Turbomachinery*, Vol. 116, pp. 721-729

Popp, O., 1999, "Steady and Unsteady Heat Transfer in a Film Cooled Transonic Turbine Cascade," PhD Dissertation, Virginia Tech.

Popp, O., Smith, D.E., Bubb, J.V., Grabowski, H.C. III, Diller, T.E., Schetz, J.A., Ng, W.F., 1999, "Steady and Unsteady Heat Transfer in a Transonic Film Cooled Turbine Cascade", ASME 99-GT-259

Rigby, M.J., Johnson, A.B., Oldfield, M.L.G., Jones, T.V., 1989,"Temperature Scaling of Turbine Blade Heat Transfer with and without Shock Wave Passing", International Symposium on Air Breathing Engines ISABE 89-7070

Rigby, M.J., Johnson, A.B., Oldfield, M.L.G., 1990, "Gas Turbine Rotor Blade Film Cooling With and Without Simulated NGV Shock Waves and Wakes", ASME 90-GT-78

Smith, D., Bubb, J., Popp, O., Grabowski, H., Diller, T., Schetz, J., Ng, W., 2000, "An Investigation of Heat Transfer in a Film Cooled Transonic Turbine Cascade, Part I: Steady Heat Transfer", ASME 2000-GT-202.